ECHO MAPPING OF ACTIVE GALACTIC NUCLEI

PhD Synopsis submitted to CHRIST (Deemed to be University)
for the award of the Degree of

DOCTOR OF PHILOSOPHY
IN
PHYSICS

by

AMIT KUMAR MANDAL
REGISTER NUMBER
1740077

Under the Supervision of

Blesson Mathew
Assistant Professor
&
C. S. Stalin
Professor
Indian Institute of Astrophysics, Bengaluru

Signature of Scholar **Signature of Research Supervisors**

CHRIST
(DEEMED TO BE UNIVERSITY)
BANGALORE · INDIA

CENTRE FOR RESEARCH
CHRIST (Deemed to be University)
BENGALURU
SEPTEMBER 2020

Centre for Research, CHRIST (Deemed to be University)

ABSTRACT

The central regions of Active galactic nuclei (AGN) are so compact and have remained elusive for direct imaging observations until recently. In the last few years, observations carried out on the European Southern Observatory's very large telescope using the technique of interferometry, were able to resolve the inner regions of AGN. However, this method is limited to nearby and bright AGN. An alternative to the direct imaging technique that also overcomes the limitations of the interferometric technique is the method of reverberation mapping (RM) or echo mapping. This technique uses the intrinsic flux variability characteristics of AGN. RM relies on the delayed response of the emission from the broad line region or the emission from the dusty torus to continuum changes from the accretion disk to find the extent of the broad line region (BLR) or the torus. This indirect method is insensitive to the distance of the AGN and in principle can be used to find the extent of the inner regions of any AGN. Using the technique of RM, in this thesis, we found the extent of the BLR to be 0.018 pc in the changing look AGN, Mrk 590. This is based on 115, 83 and 86 epochs of monitoring observations carried out in B-band, narrow Hα and SII filters, respectively. Similarly using optical and near infrared photometric monitoring observations carried out on the 2m Himalayan Chandra Telescope during the period 2016 October to 2017 April and 2017 July to 2018 December, we found the inner edge of the dusty torus in H0507+164 and Z229-15 as 0.029 pc and 0.018 pc, respectively. Our analysis carried out Z229-15 disfavours the use of constant spectral index to correct for the contribution of the accretion disk to the observed near infrared emission. We also carried out a Bayesian analysis on the RM data of 57 AGN culled from the literature to constrain the structure and kinematics of the BLR in them. As RM relies on the variability characteristics of quasars, it is imperative to observe quasars that are known to be more variable. The observational strategy of the upcoming International Liquid Mirror Telescope (ILMT) can enable one to select quasars that are variable. Towards this, from existing catalogue of quasars, we arrived at a catalogue of 6738 quasars that fall in the ILMT stripe. Many quasars in this new catalogue, can be potential candidates for RM observations in the future. This catalogue of quasars can also be used as astrometric calibrators to bring the ILMT observations in the world co-ordinate system.

Key Words: galaxies: active − galaxies: Seyfert − (galaxies:) quasars: reverberation − dust: BLR: quasars: astrometry

Contents

1 Introduction **1**

2 Review of literature **5**

3 Statement of research problem **6**

4 Objectives **7**

5 Methodology, Results and Discussion - Research work carried out **7**

5.1 The sample 7

5.2 Observations 10

5.3 Mrk 590 11

5.3.1 Data Reduction 11

5.3.2 Flux Calibration 12

5.3.3 Correction for the host-galaxy contribution 13

5.3.4 Continuum subtraction from the observed SII-fluxes 14

5.3.5 Analysis and Results 15

5.4 H0507+164 18

5.4.1 Data Reduction 18

5.4.2 Subtraction of the accretion disc component from the NIR bands 19

5.4.3 Analysis and Results 19

5.4.4 Discussion 21

5.5 Z229−15 22

5.5.1 Data Reduction 22

5.5.2 Host-galaxy contribution removal 24

5.5.3 Correction for the accretion disc contamination to the NIR flux 25

5.5.4 Analysis, Results and Discussion 26

5.6 Estimation of the size and structure of the broad line region using Bayesian approach 29

5.6.1 Analysis 29

5.6.2 Results and discussion 30

5.7 Finding quasars in the ILMT stripe 35

5.7.1 Methods followed and the resulting catalogue 35

Centre for Research, CHRIST (Deemed to be University)

5.7.2 Applications of the catalogue 37

6 Summary and future work **39**

7 Structure of the Thesis **41**

7.1 Outline of the Thesis 41

7.1.1 Chapter 1: Introduction 41

7.1.2 Chapter 2: Sample, Observations, Reduction and Analysis 41

7.1.3 Chapter 3: BLR Reverberation on Mrk 590, a changing look AGN 41

7.1.4 Chapter 4: Dust reverberation on H0507+164 and Z229−15 41

7.1.5 Chapter 5: Estimation of the size and structure of the broad line region using Bayesian approach 42

7.1.6 Chapter 6: Quasars in ILMT stripe 42

7.1.7 Chapter 7: Summary and Future prospects 42

Publications and presentations **43**

Seminars/ Conferences/Workshops attended **44**

References **46**

Centre for Research, CHRIST (Deemed to be University)

1 Introduction

Active Galactic Nuclei (AGN) are one of the most luminous objects in the universe that emit radiation covering the whole accessible bands of the electromagnetic spectrum, predominantly in X-ray, UV and optical wavelengths (Salpeter, 1964; Lynden-Bell, 1969). It is now believed that the accretion of matter on to super massive black holes (SMBHs; $10^6 - 10^{10}$ $M_\odot$) located at the centers of such galaxies, is mainly responsible to produce such high luminosity ($10^{42} - 10^{46}\,\mathrm{erg\,s^{-1}}$; Fabian, 1999). The SMBH is surrounded by an optically thick and geometrically thin accretion disc (Shakura & Sunyaev, 1973). Broad line region (BLR) that lies on scales of about ~ 0.01 pc (typical for the Seyfert category of AGN) from the accretion disc, produces the line emission due to the photo-ionization of gas clouds by the UV-optical ionizing continuum from the accretion disc. According to the unified scheme of AGN, a putative torus that surrounds the BLR region is responsible for the different manifestations of the AGN (Type 1 and Type 2), when viewed at different orientations (Antonucci, 1993; Urry & Padovani, 1995). The inner radius of the torus can extend to $0.01 - 0.1$ pc equivalent to $10 - 100$ light-days, for a typical UV luminosity of $10^{42} - 10^{46}\,\mathrm{erg\,s^{-1}}$ (Suganuma et al., 2006). So, different regions located at the central part of AGN are so compact that it is difficult to probe these regions using any current imaging techniques, except for a handful of the closest ones. A schematic representation of the different components of AGN is shown in Fig. 1.

Very few interferometric observations were done to probe the central regions of AGN. For example, Gravity Collaboration et al. (2018) observed 3C 273 using GRAVITY instrument mounted on the 8 m Very Large Telescope (VLT) and found a mean BLR size of 145 ± 35 days using Paα line through interferometric technique. Recently, from high resolution radio observations using the Very Large Array, Carilli et al. (2019) have imaged the torus in a radio galaxy Cygnus A. They found an elongated structure, perpendicular to the radio jets and centered on the core, with a full length of about 528 pc and a full width of 286 pc. GRAVITY Collaboration et al. (2019) partially resolved the size and structure of hot dust using VLTI/GRAVITY and reported the increase of the physical radius with bolometric luminosity in eight Type 1 AGN. All these interferometric observations are limited by the brightness and compactness in terms of the sizes of the regions to resolve in these objects. But this kind of limitation is not with reverberation mapping (RM) or Echo mapping method that uses the variability characteristics of AGN to probe their central regions and thus can be used to probe the central regions of AGN at comparatively higher redshift for a large number of sources.

BLR reverberation/Optical reverberation mapping is based on measuring the time delay (τ) between the UV/optical continuum from the accretion disc and the broad emission lines produced in the

Centre for Research, CHRIST (Deemed to be University)

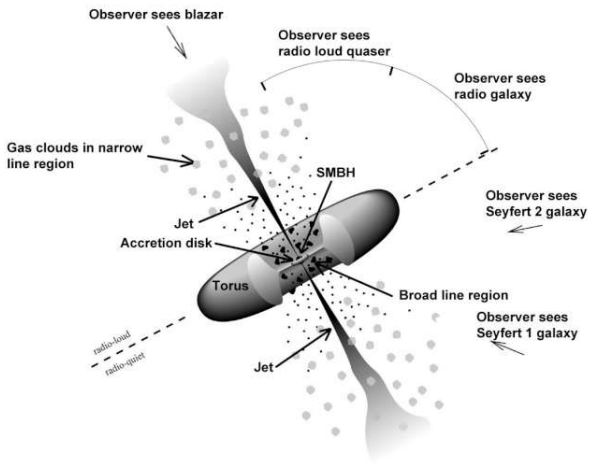

Figure 1: Unification scheme of AGN. Image courtesy: Fermi Gamma-ray Space Telescope.

BLR. The time delay (τ) can be measured using traditional cross-correlation techniques (Edelson & Krolik, 1988; Peterson, 1993) which in principle gives the average radius of the BLR ($R_{BLR} = \tau/c$, where c is the velocity of light). The mass of the black hole (M_{BH}) in an AGN can be estimated from the measured BLR size (R_{BLR}) and the width of the broad emission line (ΔV), measurable from the spectrum using the relation

$$M_{\rm BH} = f_{\rm BLR}\left(\frac{\Delta V^2 R_{\rm BLR}}{G}\right) \quad (1)$$

where G is the gravitational constant and $f_{\rm BLR}$ is the virial factor that depends on the geometry and kinematics of BLR. The method of RM has been applied to measure M_{BH} in more than 100 AGN with most of the measurements coming from the compilation[1] of Bentz & Katz (2015), the Sloan Digital Sky Survey Reveberation Measurement project (Grier et al., 2017b) and the Super-Eddington Accretion in Massive Black Holes project (Du et al., 2014, 2016, 2018; Wang et al., 2014). The $f_{\rm BLR}$ in Equation 1 can be calibrated considering the same $M - \sigma_*$ relation is applicable for both AGN and local quiescent galaxies (e.g., Onken et al., 2004; Woo et al., 2015), where σ_* represents the stellar velocity dispersion. However, it is not clear whether a constant $f_{\rm BLR}$ can be used to estimate M_{BH} for all AGN considering the complex geometry and kinematics of individual AGN because it is found that the virial factor depends on the bulge type of the host galaxy (Ho & Kim, 2014).

As of today BLR reverberation is applied to measure the size of BLR in more than 100 AGN, which leads to a linear relation between the radius of the BLR (R_{BLR}) and the continuum luminosity at 5100 Å (Wang et al., 2014; Bentz & Katz, 2015; Grier et al., 2017b), in the luminosity range between $10^{42} - 10^{46}\,{\rm erg\,sec^{-1}}$. Most of the RM studies available in literature are mainly focused on

[1] http://www.astro.gsu.edu/AGNmass/

Centre for Research, CHRIST (Deemed to be University)

estimating BLR sizes and M_{BH} which are driven by the quality of the available RM data, characterized by time resolution and signal-to-noise ratio (SNR). Using direct RM approach it is difficult to constrain the geometry and kinematics of the emitting regions unless the transfer function can be recovered. However, it is in principle possible to calculate time delays as a function of velocity across the emission line profile and better constrain the geometry and kinematics of the gas in the BLR for sources with densely sampled and good SNR spectra (e.g., Ulrich & Horne, 1996; Bentz et al., 2010; Grier et al., 2013; Xiao et al., 2018). Also, there are reports in literature that model the RM data using Bayesian approach to constrain the geometry and dynamics of the BLR by estimating different AGN parameters, as well as, $f_{\rm BLR}$ for individual objects (Pancoast et al., 2011; Brewer et al., 2011; Pancoast et al., 2012, 2014; Li et al., 2018). In addition, Li et al. (2013) developed a geometrical modelling code, PBMAP (Parallel Bayesian code for reverberation-MAPping data) providing several parameters, e.g., BLR size, inclination angle ($\theta_{\rm inc}$), opening angle ($\theta_{\rm opn}$) including non-linear response of the line emission to the continuum and allow for detrending the light curves (Welsh, 1999; Denney et al., 2010; Li et al., 2013, 2019). They applied this technique to a sample of 40 objects using archival Hβ line and continuum light curves to recover velocity integrated transfer function considering a disc-like BLR structure emitting Hβ line. Such a flattened disc like BLR is also seen in the high resolution observations of 3C 273 with the VLT (Gravity Collaboration et al., 2018). Also, there are evidences of non-linear responses of the line fluxes to the continuum (Li et al., 2013), which were ignored in the previous RM studies. It is therefore important to extend this approach to a large number of AGN to examine differences if any in the geometry of the BLR between different AGN.

A putative torus, that obscures the central engine, is the dominant source of infrared (IR) radiation showing a bump in the IR region in the broad-band spectral energy distribution (SED) (Barvainis, 1987; Sanders et al., 1989; Kobayashi et al., 1993) in most of the AGN. An analogous method to the BLR reverberation mapping experiment is the dust reverberation mapping (DRM) (Suganuma et al., 2006; Koshida et al., 2014; Mandal et al., 2018; Minezaki et al., 2019) based on the delayed response of the near infrared (NIR) radiation from dust torus to changes in the UV/optical continuum emission from the accretion disc. From NIR interferometric observations it has been found that the dust torus size do not follow the known relation $\Delta t \propto L^{0.5}$ as found in reverberation mapping program (Koshida et al., 2014), instead the half light radius $R_{1/2}$, which is defined as the radius within which half of the total integrated light at a given wavelength is contained, varies as $R_{1/2} \propto L^{0.21}$ (Kishimoto et al., 2011b). More than three dozen of AGN have been studied using DRM as of today to measure the inner radius of the dust torus (Koshida et al., 2014; Minezaki et al., 2019). Koshida et al. (2014)

Centre for Research, CHRIST (Deemed to be University)

applied DRM on 17 Seyfert 1 galaxies and published 49 measurements of lag times between the K-band flux and that of the optical continuum in the V-band for those sources. Their study reveals a systematically smaller torus size measured from DRM compared to the interferometric radius in the K band. Minezaki et al. (2019) carried out a DRM survey of quasars at redshifts $z < 0.6$ and reported torus sizes for 22 targets. They found a strong correlation between the reverberation radius of the inner dust torus and the optical V-band luminosity with a slope of 0.424, which is smaller than the value 0.5 which is theoretically expected (Koshida et al., 2014).

Moreover, combining dust inner angular size, measured by optical interferometry, with linear size measured by reverberation mapping, it has been possible to estimate direct distance, which could allow to constrain cosmological models and prove the nature of dark energy, if a dozen of objects could be observed by both techniques (Hönig et al., 2014). Both the emission line lag (Haas et al., 2011; Watson et al., 2011; Czerny et al., 2013) and dust reverberation lag (Oknyanskij et al., 1999; Oknyanskij & Horne, 2001; Hönig et al., 2014; Yoshii et al., 2014; Hönig & Kishimoto, 2017) have been proposed to serve as standard candles. However, a stronger correlation between dust-lag and luminosity needs only photometric monitoring making it preferable for standard candle, although the emission line lags can be measured up to $z \sim 4$ (see Watson et al., 2011). Unfortunately, there are a few objects having dust lag measurement (Suganuma et al., 2006; Koshida et al., 2014; Pozo Nuñez et al., 2014), which motivated Hönig & Kishimoto (2017) to carry out a large DRM program, 'VEILS' (VISTA Extragalactic Infrared Legacy Survey) to use dust lag as standard candle for cosmology and constrain cosmological parameters from a survey of about 1350 Seyfert 1 galaxies in the redshift range $0.1 < z < 1.2$. They, however, missed the objects in the local universe, which are crucial in determining the normalization parameter of the AGN distance moduli (see Hönig & Kishimoto, 2017). There are only about 20 AGN (Suganuma et al., 2006; Koshida et al., 2014; Mandal et al., 2018) studied for DRM program in the local universe with redshift < 0.1.

Long-term study of variability properties of AGN/quasars is very crucial in reverberation mapping program. For this purpose a dedicated telescope is needed to monitor large number of AGN/quasars over long duration of time. The 4m International Liquid Mirror Telescope (ILMT) which will observe in the Time Delayed Integration (TDI) mode is expected to be commissioned soon on the Aryabhatta Research Institute of Observational Sciences (ARIES) site in Devasthal, India (Surdej et al. 2018). The ILMT which will be repeatedly scanning the sky within a narrow stripe of width $\sim 27'$, can play an important role to study optical variability properties of AGN/quasars falling in the ILMT stripe. Beside, to convert the observations from the pixel coordinate system to the world coordinate system

Centre for Research, CHRIST (Deemed to be University)

(α, δ) we need to carry out astrometric calibration of the ILMT fields. For that, we choose quasars as astrometric standards because of their negligible proper motions (PM) and trigonometric parallaxes to construct a catalogue of quasars that will be used to carry out astrometric calibration of the ILMT fields. The resulting ILMT quasar (IQ) catalogue can be used to study optical flux variability and colour variability properties which will in turn can be used as the primary requisites of reverberation mapping program.

Since the discovery of AGN, the progress in revealing the inner parts of AGN came with the advancement of observing facilities like telescopes, satellites, detectors as well as improvements in theoretical models. This thesis aims to probe the inner regions of AGN, that could pave the way for improved understanding of their central regions.

2 Review of literature

Because of compactness of the central regions in AGN, it is difficult to probe those regions using any current direct imaging techniques. One of the important characteristics of AGN is that they show flux variability over the entire electro-magnetic spectrum (Wagner & Witzel, 1995; Ulrich et al., 1997). This flux variability property of AGN can be used to probe the spatially unresolved inner regions in them. A method that relies on this flux variability property, used to probe different emitting regions in the central part of AGN is the Reverberation mapping technique which was first introduced by Blandford & McKee (1982). Since then, many observational and theoretical efforts were done to reveal the structure and kinematics of the central part of AGN using reverberation mapping (Ulrich & Horne, 1996; Bentz et al., 2010; Grier et al., 2013; Xiao et al., 2018).

The various observational efforts that are devoted to probe the central regions of AGN fall under the following three categories.

1. **Program to find the extent of the BLR (and subsequently the black hole mass) via BLR reverberation mapping:** This is usually accomplished by spectroscopic monitoring observations. However, over the last few years, photometric monitoring observations through suitable selection of narrow band filters that could cover the emission line coming from the BLR and the continuum from the central region, has been attempted as an alternative to spectroscopic monitoring observations. RM measurements of the size of the BLR are now available more than 100 AGN, but this study is limited to sources that cover a small range of redshift and luminosity. Most of such measurements are from the compilation of Bentz & Katz (2015), the Sloan Digital Sky Survey Reverberation Measurement project carried out by Grier et al. (2017b) and

Centre for Research, CHRIST (Deemed to be University)

the Super-Eddington Accretion in Massive Black Holes project by Wang et al. (2014); Du et al. (2016); Li et al. (2018); Xiao et al. (2018).

2. **Program to find the extent of the dusty torus:** This is accomplished by photometric monitoring of AGN in the optical and NIR bands and then use the time delay between the optical and IR light curves to indirectly find the extent of the inner edge of the dusty torus. This has been carried out for about 40 objects. Recently, Lyu et al. (2019) using optical and mid infrared (MIR) observations, reported results of the size of the torus for most of the Palomar-Green quasars and found the MIR time lags to follow the relation $\Delta t \propto L^{0.5}$, and increase in average torus size with wavelength. And for most of the objects for which dust torus size is available, the light curves used to find the lag are not well sampled in time (Koshida et al., 2014; Minezaki et al., 2019).

3. **Direct imaging of the central region:** In addition to the above two indirect ways to find the extent of different components in AGN, direct imaging observations too are now possible using sensitive instruments on the currently operating large optical/IR telescopes in the world. But this is limited to only a handful of very nearby and bright objects, made possible by interferometric techniques. The inner extent of the dust torus via interferrometry is now known for about two dozen AGN (Kishimoto et al., 2009, 2011a; GRAVITY Collaboration et al., 2019; Gravity Collaboration et al., 2020). Moreover, combining dust inner angular size measured by optical/IR interferrometry with linear size measured by reverberation mapping it has been possible to estimate direct distance. This could allow to constrain cosmological models and prove the nature of dark energy if a dozen objects spanning a wide range of redshifts could be observed by both techniques (Hönig et al., 2014).

3 Statement of research problem

From the brief overview of the current observational status on the indirect method of using reverberation mapping (RM) to probe the central regions of AGN, it is evident that one needs to increase the number of sources with better RM based measurement of BLR size and dust torus size. Any progress in this direction is contingent upon carrying out of good quality (time sampling and S/N) observations of more number of AGN. The key ideas that we aim to pursue in this thesis work are

1. How does the the BLR size estimated from photometric monitoring observations compare with that obtained from spectroscopic reverberation mapping observations?

Centre for Research, CHRIST (Deemed to be University)

2. How do new measurements on the inner extent of the dust torus fit into the already existing dust lag v/s luminosity relation? This involves measurement of the torus size in more AGN.

3. From modelling of the observed light curves, one can infer the geometry and kinematics of the BLR. Based on modelling approach, how do the geometry and kinematics of BLR compare among different sources?

4. How many known quasars are there in the ILMT stripe? What is their usability as astrometric standards?

   These questions will be addressed in this thesis.

4 Objectives

Based on the key research problems stated above in reverberation mapping study in AGN, the main objectives of the thesis are as follows

1. Measurement of the size of BLR and black hole mass using narrow band photometric monitoring.

2. Determination of the size and structure of dust torus in AGN through optical and NIR photometric monitoring.

3. Estimation of the size and structure of the BLR region using Bayesian statistics through theoretical model.

4. Finding quasars in the ILMT stripe and their usability as astrometric calibrators.

5 Methodology, Results and Discussion - Research work carried out

5.1 The sample

1. **BLR reverberation:**

   Photometric monitoring of AGN have started to emerge as an alternative method to the conventional spectroscopic monitoring of AGN to find the extent of the BLR. Such a program demands a careful selection of the target so that the continuum and line fall on the set of broad/narrow band filters available at any observing facility. For this objective, we have carefully selected the source Mrk 590 whose redshifted Hα falls in the narrow filter centered at SII region and

Centre for Research, CHRIST (Deemed to be University)

the continuum falls on the broad B-band. This source is a changing look AGN at a redshift z = 0.0264.

2. **Dust Reverberation:**

   The size of the inner edge of dust torus is known for about three dozen AGN. Most of these measurements are based on sparsely sampled optical and near-infrared observations. A possible reason for the paucity of such data could be due to the difficulty in scheduling observations in the optical and NIR bands, simultaneously. To increase the measurements of dust torus size in AGN, we have initiated a program called REMAP (REverberation Mapping of AGN Program). The initial sample of sources for monitoring under REMAP were selected as follows.

   (i) Firstly, we used the sample of 60 sources for which RM of BLR were available (Bentz & Katz, 2015). This is because, there are only a few sources for which the time lag measurements for both BLR and the torus are available. Comparisons of these measurements indicate that the torus lag is $4-5$ times larger than the BLR lag.

   (ii) Secondly, we imposed the condition that the BLR lag should be greater than 3 days and lesser than 10 days. This condition was guided by our ability to observe each source once every five days, which sets the time resolution of our data. With this time resolution it would be possible to obtain meaningful lag only for those sources that are expected to have dust lag more than 30 days or so and monitored for a duration of about 6 months.

   (iii) Thirdly, the sources must be brighter than 16.5 magnitude in the V-band and must have declination greater than -10 degree. The magnitude constraint was imposed so as to get good S/N data within our allocated time at the Himalayan Chandra Telescope (HCT) and the declination limit is for the observability of sources from HCT.

   The above selection criteria lead us to a final sample of 8 sources for REMAP. The details of these sources are given in Table 1.

   For this thesis work, I concentrated on the brightest two sources in this sample, namely H0507+164 and Z229$-$15.

3. **Estimation of the size and structure of the broad line region using Bayesian approach**

   In order to estimate the black hole masses and study the accretion mechanism in AGN it is important to understand the kinematics and geometry of the BLR of AGN. From high signal to noise ratio spectra and using the technique of velocity resolved reverberation mapping it

Centre for Research, CHRIST (Deemed to be University)

Table 1: Details of the initial list of objects selected for the REMAP monitoring.

No.	Object Name	RA (2000)	DEC (2000)	V (mag)	z	Type	M_{BH} ($\times 10^6 M_\odot$)	R_{BLR} (days)
1	H0507+164	05:10:45.5	+16:29:56	15.64	0.018	Seyfert 1.5	$9.62^{+0.33}_{-3.73}$	$3.01^{+0.42}_{-1.84}$
2	Z 229-15	19:05:25.9	+42:27:40	15.40	0.028	Seyfert 1	$10.00^{+1.90}_{-2.40}$	$3.86^{+0.69}_{-0.90}$
3	Mrk 142	10:25:31.3	+51:40:35	16.15	0.045	Seyfert 1	$2.17^{+0.77}_{-0.83}$	$2.74^{+0.73}_{-0.83}$
4	MCG+10-16-111	11:18:57.7	+58:03:24	16.71	0.028	Seyfert 1	$5.50^{+2.00}_{-1.80}$	$2.31^{+0.62}_{-0.49}$
5	Arp 151	11:25:36.2	+54:22:57	16.49	0.021	Seyfert 1	$6.41^{+0.92}_{-1.19}$	$3.99^{+0.49}_{-0.68}$
6	Mrk 1310	12:01:14.3	−03:40:41	15.91	0.019	Seyfert 1	$2.20^{+0.90}_{-0.90}$	$4.20^{+0.90}_{-0.10}$
7	Mrk 202	12:17:55.0	+58:39:35	16.41	0.021	Seyfert 1	$1.30^{+0.40}_{-0.40}$	$3.50^{+0.10}_{-0.10}$
8	NGC 5273	13:42:08.3	+35:39:15	13.12	0.003	Seyfert 1	$4.70^{+1.60}_{-1.60}$	$2.21^{+1.19}_{-1.60}$

is possible to infer the geometry and kinematics of the BLR. However, such observations are available for only limited number of AGN. Li et al. (2014) performed light curve modelling on the velocity resolved RM data of NGC 5548 based on Bayesian method. An alternative to this approach is to use conventional reverberation mapping data in a theoretical formalism to get the geometry and kinematics of BLR. Thus to infer the geometry of a large sample of AGN, we modelled the emission and continuum light curves for a sample of 58 objects using a Markov Chain Monte Carlo method based on Bayesian statistics and implemented in PBMAP (Parallel Bayesian code for reverberation MAPping data). This sample was arrived at by retrieving data for all objects from the literature and imposing two additional constraints (i) the sources must have the continuum and line light curves and (ii) there is no previous investigation of the BLR structure for the objects. Based on the above two criteria we arrived at a sample of 58 objects.

4. The ILMT quasar (IQ) catalogue

To select all known quasars that are available in the ILMT stripe and their subsequent use for the calibration of ILMT observations, we looked at the suitability of all quasar catalogues that are available in the literature. One such quasar catalogue suited for our purpose is the Million Quasars (Milliquas) catalogue by Flesch (2017), the largest compilation of quasars available as of today. This catalogue contains about 1998464 quasars taken from different quasar surveys. The majority of quasars in the Milliquas catalogue are from the The Sloan Digital Sky Survey (SDSS), one of the ambitious sky surveys covering more than a quarter of the sky in the northern hemisphere in five optical filters. Other quasars included in Milliquas come from the NBCKDE, NBCKDE-v3 (Richards et al., 2009, 2015), XDQSO (Bovy et al., 2011; Myers et al., 2015), All-

Centre for Research, CHRIST (Deemed to be University)

WISE and Peters photometric quasar catalogues (Peters et al., 2015), as well as quasars from all-sky radio/X-ray surveys. The Milliquas catalogue is a compilation of quasars from different surveys with varied uncertainties in the equatorial coordinates. But one needs to have quasars with precise positions with uncertainties to carry out astrometric calibration. The only source that provides precise positions in equatorial coordinates of celestial sources is the survey being presently carried out by the European Space Agency *Gaia* mission. *Gaia*-DR2 (Lindegren et al., 2012; Gaia Collaboration et al., 2018) contains data from the all sky astrometric and photometric survey conducted by *Gaia* and provides accurate positions for about 1.7 billion sources, with proper motion (PM) and parallax measurements for about 1.3 billion sources (Marrese et al., 2019). Therefore, to get accurate positions for the quasars in the Milliquas catalogue we used the precise and homogeneous measurements from *Gaia*-DR2.

5.2 Observations

1. **BLR Reverberation**

   The photometric observations of Mrk 590 were carried out in the optical B and narrow SII-band over 115 and 83 epochs, respectively, during the period July, 2018 to December, 2018. The redshifted Hα line falls in narrow SII-band whereas B-band contains the continuum flux from accretion disc. The average readout noise and gain of the CCD used are 10.21 electrons and 2.2 electrons/ADU, respectively. The typical exposure time in B and narrow SII bands are about 240s and 900s, respectively.

2. **Dust Reverberation**

   As part of the REMAP project (Mandal et al., 2018, 2019), the two sources studied in this thesis, namely H0507+164 and Z229−15 were monitored using the 2 m Himalayan Chandra Telescope (HCT) at Hanle, India, operated by the Indian Institute of Astrophysics, Bangalore. The telescope is a Ritchey−Chretien system with an f/9 beam. The optical observations were carried out using the Himalayan Faint Object Spectrograph and Camera (HFOSC) mounted at the Cassegrain focus and equipped with a 2K $\times$ 4K SiTe CCD system. This CCD has a readout noise and gain of 4.8 electrons and 1.22 electrons/ADU, respectively. The observations were carried out in binned mode using only the central 2K $\times$ 2K region. Each pixel of the CCD in this mode corresponds to 0.3 $\times$ 0.3 arcsec^2 , and for the imaging observations reported here has a field of view of 10 $\times$ 10 arcmin^2. The NIR observations were done using the TIFR Near Infrared Spectrometer (TIRSPEC) mounted on one of the side ports of HCT (Ninan et al.,

Centre for Research, CHRIST (Deemed to be University)

2014). The detector used in TIRSPEC is a 1024 × 1024 HgCdTe array with a pixel size of 18 μm covering a field of view of 5 × 5 arcmin^2. It has a readout noise and gain of 25 electrons and 6 electrons/ADU, respectively. The NIR observations were performed in dithered mode of five exposures each of 20 s at three dither positions for each of three NIR filters, namely J, H, and K_s. Apart from the science frames, sky regions were also observed in the same dithering pattern as the object to generate master sky frame.

For H0507+164, the observations were carried out for a total of 35 epochs during the period 2016 October to 2017 April in optical V-band and NIR J, H and K_s-bands, simultaneously using HCT. The typical exposure time in V band is about 50 s. The NIR observations in J, H, and K_s bands were done subsequently to the V-band observations at each epoch using the TIRSPEC.

We monitored Z 229-15 photometrically in optical B and V bands and NIR J, H, K_s during the period 2017 July to 2018 December for a total of 48 epochs using HCT. The average exposure time in V-band is about 50 s. As AGN do show spectral variability with a bluer-when-brighter behaviour (Meusinger et al., 2011), which demands adoption of a time dependent power-law index to correct for the contribution of accretion disc emission to NIR, 1 exposure of 150 sec in B band was taken subsequent to the V-band observation at each epoch.

The details related to the data reduction, flux calibration and obtained results for each object are mentioned below:

5.3 Mrk 590

5.3.1 Data Reduction

The data reduction for Mrk 590 was done using IRAF (Image Reduction and Analysis Facility) for the B-band and narrow Hα and SII-band data. We followed the standard procedures for image reduction, such as bias & dark subtraction and flat-fielding. We performed aperture photometry on the images for B, Hα and SII-band data.

We adopted growth curve method for photometry in B, Hα and SII-band data. The instrumental magnitudes were obtained in several concentric apertures centered on the point source for one comparison star with the best S/N present in the same field of view (FoV) of the target source. The growth curve is produced by plotting the instrumental magnitude within each aperture with aperture size as shown in Fig. 2. The growth curve increases with aperture till the aperture is large enough to capture three sigma of the present signal and becomes linear with a slope based on the image background. We

Centre for Research, CHRIST (Deemed to be University)

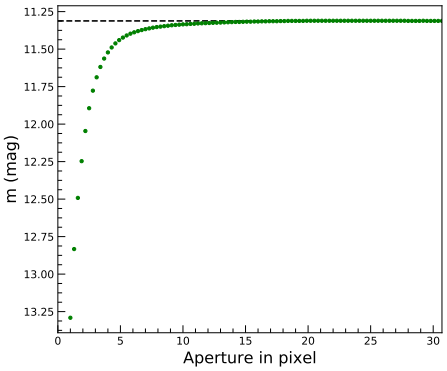

Figure 2: Growth curves for the comparison star in SII-band. The dashed black line represents the best fit line corresponding to the points with aperture size more than 3 times the FWHM.

fit a linear line based on the method of least squares to the portion of the growth curve with apertures beyond three times the FWHM of the comparison star. The intercept of the fitted line is taken as the desired instrumental magnitude which corresponds to a particular optimum aperture. We used the same optimum aperture obtained for the comparison star to find the instrumental magnitude of the target source. This method was applied to each epoch to get the instrumental magnitudes of the target and the comparison star present in the CCD frames for all the B, Hα and SII-band data.

5.3.2 Flux Calibration

We used differential photometry to convert the instrumental magnitudes obtained from aperture photometry in broad B band and narrow Hα and SII bands into fluxes using the following steps:

1. We retrieved u and g-band apparent magnitudes for one comparison star with best S/N from the same observed field of Mrk 590 from SDSS database. B-band apparent magnitude of that comparison star was obtained using SDSS u and g- magnitudes as given below [2]:

$$B = u - 0.8116(u - g) + 0.1313 \tag{2}$$

   Then the obtained B-band instrumental magnitude of the target Mrk 590 was converted to standard B-band magnitude with respect to the comparison star using differential photometry . This apparent magnitude was then converted to B-band flux using the conversion factor given in Bessell et al. (1998).

[2] https://www.sdss.org/dr12/algorithms/sdssUBVRITransform/#Lupton2005

Centre for Research, CHRIST (Deemed to be University)

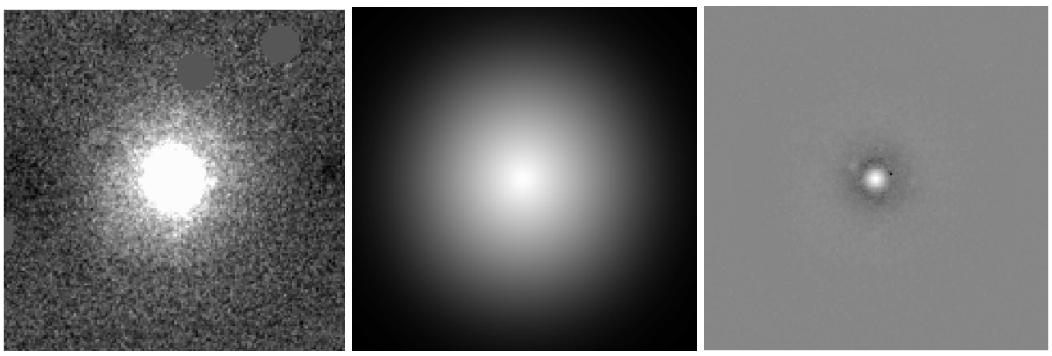

Figure 3: Observed SII-band image of Mrk 590 (left), modeled galaxy image (middle) and residual image containing the AGN at the center (right) obtained from GALFIT. The modeled and residual images are displayed with a logarithmic stretch.

2. The mean wavelengths of narrow Hα and SII-filter are approximately 6563 and 6719 Å (Andjelić et al., 2011), respectively. The SDSS r-band has wavelength range from 5380 Å to 7230 Å with the central wavelength at 6166 Å. So, both narrow Hα and SII bands completely fall on the SDSS r-band. So, we retrieved r-band apparent magnitudes of the comparison star from SDSS database and obtained the Hα and SII-band apparent magnitudes of the target source with respect to the comparison star using differential photometry. We used SDSS r-band conversion factor to convert the Hα and SII-band magnitudes to fluxes [3].

   The obtained apparent magnitudes were corrected for Galactic extinction, using the values taken from the NASA/IPAC Extragalactic data base (NED) for broad B band and narrow Hα and SII-bands.

5.3.3 Correction for the host-galaxy contribution

There is a prominent host galaxy contribution to the AGN flux in broad B band and narrow Hα and SII-bands, see Fig. 3 (left) for SII-band data. The two dimensional image-decomposition program GALFIT developed by Peng et al. (2002) was used to the observed B, Hα and SII-band images to estimate the host-galaxy contribution. We combined 10 frames of different epochs with good seeing condition covering the whole span of our monitoring period to obtain a single image with better S/N for each of the three bands separately. Then we applied the GALFIT on the combined images.

Kim et al. (2017) modelled Mrk 590 using GALFIT and found that the host galaxy has a pseudo bulge with Sérsic index n = 1.04 and a disc. An exponential disc profile is simply a Sérsic profile with an index of n = 1. So, we used exponential disk profile to model the underlying galaxy. We generated

[3] https://www.sdss.org/dr12/algorithms/fluxcal/

Centre for Research, CHRIST (Deemed to be University)

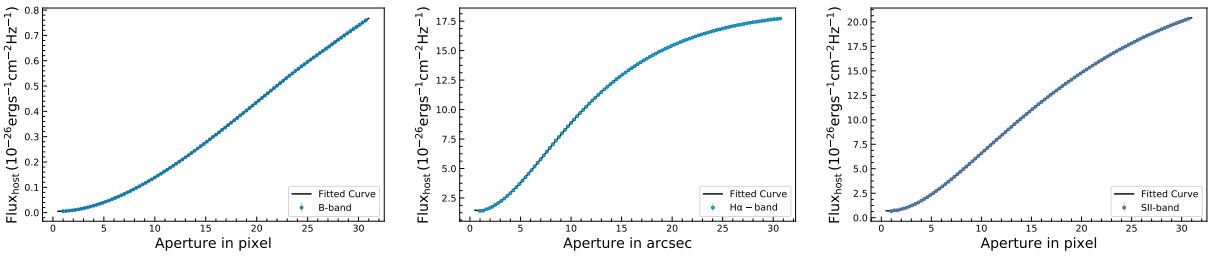

Figure 4: Host-galaxy flux as a function of aperture size in B-band (left), Hα (middle) and SII-band (right). The points with error bar are the galaxy-flux values and the solid black lines are the best polynomial fits.

PSF image from the same FoV. The modeled galaxy image and the residual image that contains the AGN for SII-band are shown in Fig. 3 (middle) and (right), respectively.

We applied aperture photometry on the modeled galaxy image at different concentric aperture sizes and the obtained galaxy-fluxes are plotted against aperture, as shown in Fig. 4, where the black solid lines represent the best-fit curve for B (left), Hα (middle) and SII (right) bands. We obtained the host-galaxy fluxes from the best fit curve at the same size of aperture used at individual epoch described in the previous section in both B and SII bands. Then we subtracted the host-galaxy fluxes from the observed total fluxes in those filters to get the AGN contribution.

5.3.4 Continuum subtraction from the observed SII-fluxes

The observed narrow SII-band images contain both Hα line and continuum fluxes. The variable continuum is mainly coming from the accretion disc and this accretion disc contamination to the observed SII-band fluxes would make the derived lag between the optical continuum and Hα line shorter than the actual true lag (Koshida et al., 2014). So, it is required to remove the accretion disc contamination to the observed line fluxes to get the actual time lag between the optical B-band continuum from accretion disc and Hα fluxes, coming from the BLR. The narrow Hα band that lies close to the narrow SII band, contains only continuum flux from accretion disc. So, the continuum contamination in the narrow SII band can be removed by directly subtracting the narrow Hα flux from the observed SII-band flux to get the Hα line flux alone.

The continuum contribution from accretion disc to the observed SII-band flux can also be evaluated using a power-law spectrum of the accretion disc given by Koshida et al. (2014):

$$f_{\mathrm{SII,continuum}}(t) = f_{\mathrm{B}}(t)\left(\frac{\nu_{\mathrm{SII}}}{\nu_{\mathrm{B}}}\right)^{\alpha_\nu} \tag{3}$$

Centre for Research, CHRIST (Deemed to be University)

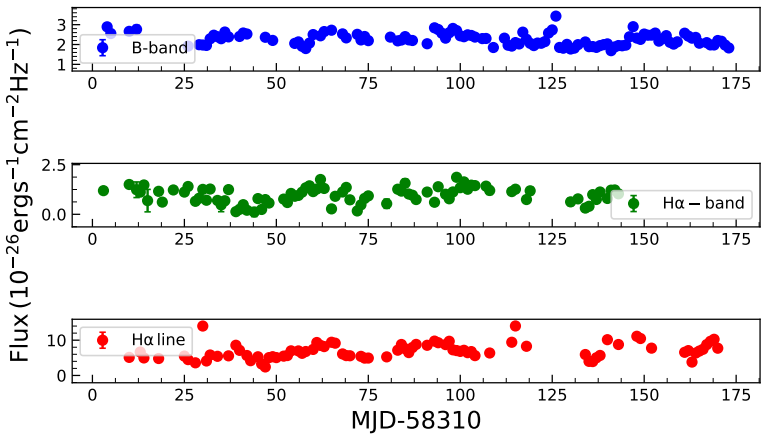

Figure 5: The light curves of Mrk 590 in B, narrow Hα band and for Hα line during the period from July, 2018 to December, 2018. The continuum contribution was subtracted from the SII-band light curve using narrow Hα band flux.

where $f_{\rm SII,continuum}$(t) and $f_{\rm B}$(t) represent the continuum flux of the SII-band from accretion disc and the B-band flux at time t, respectively. ν_B and $\nu_{\rm SII}$ are the effective frequencies of B and narrow SII bands, respectively, and α_ν is the power-law index. According to Tomita et al. (2006), the power-law index of the accretion-disc component of the flux in optical and near-infrared may vary from -0.1 to $+0.4$. Kishimoto et al. (2008) found $\alpha_\nu = 0.44 \pm 0.11$ from spectropolarimetric observations. Using the quasar composite differential spectrum observed by the Sloan Digital Sky Survey, Wilhite et al. (2005) obtained a power-law index of $\alpha_\nu = 0$. So we separately calculated the continuum contribution in the SII-band flux for $\alpha_\nu = 1/3$ as prescribed by the standard accretion disc model (Shakura & Sunyaev, 1973) and $\alpha_\nu = 0$. So, we also subtracted the $f_{\rm SII,continuum}$ from the observed SII-flux to get the Hα line flux. The obtained light curves in different bands are shown in Fig. 5 where Hα line light curve is obtained by directly subtracting the narrow Hα flux from observed SII flux to correct for the accretion disc contamination. We estimated the errors in the final flux values in B and SII bands using the method of propagation of errors (Bevington & Robinson, 1992) during various steps of flux determination.

5.3.5 Analysis and Results

1. Light curves

   The final light curves of Mrk 590 in B, narrow Hα bands and for Hα line are shown in Fig. 5. The source, a Seyfert galaxy is radio-quiet and hence there is negligible contamination from the radio jet to the observed flux variations . The different variability parameters associated with

Centre for Research, CHRIST (Deemed to be University)

Table 2: Variability statistics in B, Hα bands and for Hα line in the observer's frame where $\lambda_{\rm eff}$ is the effective wavelength in Angstroms. The average values ($< f >$) and the standard deviation σ of the light curves are in units of $10^{-26}\,{\rm erg\,s^{-1}\,cm^{-2}\,Hz^{-1}}$. The luminosities in each band are in erg s^{-1}.

Filter	λ_{eff}	$< f >$	σ	F_{var}	R_{max}	log $L_{\rm host}$	log $L_{\rm AGN}$
B	4363	2.26 ± 0.05	0.31	$0.132 \pm < 0.001$	2.03	42.22 ± 0.01	43.36 ± 0.01
$H\alpha$	6563	0.97 ± 0.13	0.40	0.379 ± 0.005	16.60	$43.85 \pm < 0.01$	42.81 ± 0.06
$H\alpha$ line	6564.6	6.93 ± 0.18	2.19	$0.315 \pm < 0.001$	5.82	$43.70 \pm < 0.01$	43.67 ± 0.01

the light curves are mentioned in Table 2, where F_{var} represents the normalized excess variance (Edelson et al., 2002; Vaughan et al., 2003; Rani et al., 2017). The uncertainties in the F_{var} were evaluated following Edelson et al. (2002). R_{max} and σ are the ratio between the maximum and minimum flux and standard deviation of the light curves, respectively. The obtained host galaxy ($L_{\rm host}$) and AGN luminosity ($L_{\rm AGN}$) calculated from the average fluxes of the host galaxy and AGN, respectively, are also mentioned in Table 2.

2. Cross-correlation function (CCF) analysis

As the light curve of the target source Mrk 590 clearly shows flux variations, we tested for the presence/absence of time delay between B and Hα line light curves. To calculate the time lag between the variations in the optical B-band continuum coming from the accretion disc and the Hα line from the BLR, we employed two well-known methods, namely the interpolated cross-correlation function (ICCF; Gaskell & Sparke (1986), Gaskell & Peterson (1987)) and the discrete cross-correlation function (DCF; Edelson & Krolik (1988)). As total span of SII-band data is $\sim$ 160 days, first to locate the peak of CCF, we evaluated CCF in the range -50 days to +50 days so that the total duration of observing time should exceed at least 3 times larger than the expected maximum lag (Peterson & Horne, 2004), as illustrated in the Fig. 6. From Fig. 6 (left) we see that there are two peaks in the CCF, one is at around -6 days and another is at around +22 days. As negative lag here is physically not possible, so to find the expected BLR lag between B-band and Hα line, we used here the centroid of the CCF around the positive peak at +22, which is evaluated by considering the points that are within 80 per cent of the maximum of the CCF as shown in Fig. 6 (right).

We used a model independent Monte Carlo simulation based on the flux randomization (FR)

Centre for Research, CHRIST (Deemed to be University)

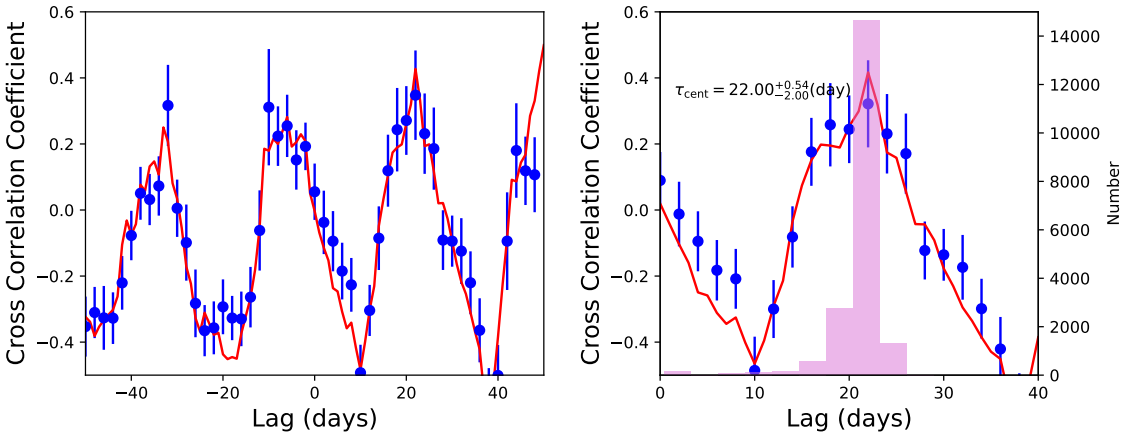

Figure 6: (Left) The CCFs between B and Hα line considering the maximum and minimum delay of +50 and -50 days, respectively. (Right) The CCFs between B and Hα line flux. The distribution of the τ_{cent} obtained using 20000 Monte Carlo Simulations is shown by histogram. The value of τ_{cent} obtained from the median of CCCD using Monte Carlo simulation based on ICCF is also mentioned in the panel. The solid red line represents the ICCF, points with error bars show the DCF obtained using $\tau = 1$ day in each panel.

and random subset selection (RSS) (Peterson et al., 1998) with some additional improvements as suggested by Wandel et al. (1999) and Peterson et al. (2004) to estimate the uncertainties in the obtained lag. For each iteration in the Monte Carlo simulation, we first randomly selected N points independent to each other from a parent light curve consists of N data points regardless of whether any point has previously been selected as suggested in RSS method. After RSS method the new light curve contains M data points. Then we applied FR method to take into account the uncertainty in the measured fluxes by randomly modifying the fluxes of the M data points including the uncertainties of the measured flux multiplied with a random Gaussian value. For each iteration in the Monte Carlo simulation, we evaluated the CCF of the modified light curve and τ was calculated using the points within 80% of the peak of the CCF. This whole process was repeated for 20 000 iterations keeping only those CCF with peak value $>$ 0.4 to have a significant cross-correlation result. The histogram shows the cross-correlation centroid distribution (CCCD) and the lag is calculated from the median of the CCCD. As the distribution has a non-Gaussian shape, the uncertainties were evaluated within 68% confidence interval around the median value.

The obtained lags with their uncertainties between B-band and Hα line in the observed frame evaluated from the Monte Carlo simulation based on ICCF analysis method is given in Table

Centre for Research, CHRIST (Deemed to be University)

Table 3: Values of τ_{cent} with errors in days as obtained by ICCF methods in observer's frame.

approach	ICCF (days)
direct observations	$22.00^{+0.54}_{-2.00}$
power-law spectrum of AD	$22.00^{+0.96}_{-1.07}$

6 considering narrow Hα-band flux as accretion disk contamination in SII-band fluxes and assuming a power-law spectrum with α = 1/3. We could not find any change in the derived lag for those two different approaches. The redshift corrected rest frame time lag between B band and Hα line is found to be $21.44^{+0.53}_{-1.95}$ days. So, the obtained mean BLR size based on the lag between continuum in B-band and Hα line for Mrk 590 is $21.44^{+0.53}_{-1.95}$ days which is equivalent to 0.018 pc. This measured lag of 21.44 days based on photometric reverberation between Hα and continuum is similar to the value of $20.7^{+3.5}_{-2.7}$ days obtained by spectroscopic monitoring observations of the same source using the Hβ line (Bentz et al., 2013).

5.4 H0507+164

5.4.1 Data Reduction

The optical data of H0507+164 was reduced using IRAF and MIDAS (Munich Data Analysis System). After correcting for bias and flat, the science frames were obtained. We removed the cosmic rays using MIDAS and the optical frames were aligned and then combined using *imalign* and *imcombine* tasks in IRAF for each day. Point spread function (PSF) photometry was carried out on the combined images using the DAOPHOT and ALLSTAR packages in MIDAS to find the instrumental magnitudes of the object and the comparison stars present in the CCD frames.

We used TIRSPEC NIR Data Reduction Pipeline (Ninan et al., 2014) to reduce the NIR data for each band by subtracting the dark obtained for the same exposure time as the science exposures and then used twilight flats for flat fielding and produced the final combined images. PSF photometry was performed on the combined images using MIDAS to get the instrumental magnitudes.

The object appears as a point source in our optical and IR data, thereby, making it difficult to model the host galaxy from the observed data and remove its contribution to the measured brightness. Therefore, subtraction of the host galaxy contribution to the measured brightness of the source was not performed.

Centre for Research, CHRIST (Deemed to be University)

5.4.2 Subtraction of the accretion disc component from the NIR bands

The NIR flux is mainly coming from the torus due to the irradiation of the hot dust particle by the optical/UV ionizing continuum from accretion disc. But there is a contribution of variable NIR continuum emission from the accretion disc to the observed NIR flux (Tomita et al., 2006; Kishimoto et al., 2008; Lira et al., 2011). This accretion disc contamination to the NIR flux makes the derived lag between the optical/UV continuum and NIR continuum shorter than the actual lag (Koshida et al., 2014). So to get the actual time lag, between optical and NIR flux variations, the contribution of the accretion disc to the observed NIR fluxes needs to be removed. The accretion disc contribution of the NIR flux was evaluated considering a power-law spectrum of the accretion disc given by Koshida et al. (2014):

$$f_{NIR,disc}(t) = f_V(t)\left(\frac{\nu_{NIR}}{\nu_V}\right)^{\alpha} \quad (4)$$

where $f_{NIR,disc}(t)$ and $f_V(t)$ represent the accretion disk component of the NIR flux and the V-band flux at time t, respectively. ν_V and ν_{NIR} are the effective frequencies of V, NIR (J, H, K_s) bands, respectively, and α_ν is the power-law index. We used power-law index α to be equal to 1/3 following Koshida et al. (2014) to calculate $f_{NIR,disc}(t)$. As AGN shows spectral variability with a bluer-when-brighter behaviour (Meusinger et al., 2011), we should consider a time dependent α to correct for the accretion disc contamination to NIR. But we are limited by our single optical V-band observations which hindered determination of α for each epoch of our observations.

5.4.3 Analysis and Results

1. Light curves

   The light curves of H0507+164 in optical V band and NIR J, H, and K s bands are illustrated in Fig. 7 (left). As the source is radio-quiet, not much contamination to the observed flux variations is expected from the jet of the source.

2. Cross-Correlation Analysis

   We applied both DCF and ICCF as described in Section 4.3.5 to find the time lag between the variations in the optical V band and different NIR bands. In order to estimate the uncertainties in the measured lags we stuck to the same procedure as followed in Mrk 590 with the condition that the Monte Carlo simulation was repeated for 20 000 iterations including only those CCF having peak value > 0.5 so that the cross-correlation result is significant. The obtained CCFs

Centre for Research, CHRIST (Deemed to be University)

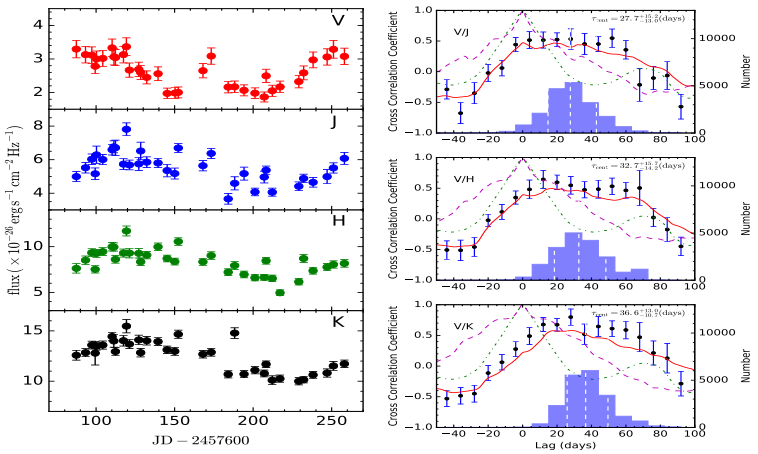

Figure 7: Left: The light curves of H0507+164 in V, J, H, K_s bands for the period from 2016 October to 2017 February. The NIR light curves were corrected for the accretion disc contamination. Right: The CCF of V versus J (top panel), V versus H (middle panel), and V versus K (bottom panel) is shown. The solid line represents the ICCF while the points with error bars show the DCF obtained using τ = 5 days and the distribution of the $\tau_{\rm cent}$ obtained using 20 000 Monte Carlo Simulations. The dashed−dot line represents the ACF of V-band light curve and the dashed lines are the ACF of corresponding NIR band light curves. The value of $\tau_{\rm cent}$ obtained using Monte Carlo simulation is noted in each panel.

between the optical V-band and the different NIR bands and their corresponding CCCD are shown in Fig. 7 (right).

Based on the above approach, we estimated the rest frame (corrected for the redshift) time lags of $27.1^{+13.5}_{-12.0}$ days between V and J bands, $30.4^{+13.9}_{-12.0}$ days between V and H bands, and $34.6^{+12.1}_{-9.6}$ days between V and K_s bands. Though there is a hint of wavelength dependent lag, that increases with wavelength, we conclude that within errors, the derived lags are consistent with each other. We obtained a time lag of $34.6^{+12.1}_{-9.6}$ days which is considered as the representation of the size of the dust torus in H0507+164 with K_s band variation lagging the V-band variations. This lag is found to be larger than the lag of $3.01^{+0.42}_{-1.84}$ days obtained between the optical continuum and Hβ emission line from optical monitoring observations by Stalin et al. (2011). The obtained lags between optical V-band and different NIR bands in observer's frame are given in Table 4.

Centre for Research, CHRIST (Deemed to be University)

Table 4: Values of $\tau_{\rm cent}$ and their associated erros in days as obtained by DCF (for various bin size ($\Delta\tau$)) and ICCF methods in observer's frame.

Bands	DCF ($\Delta\tau$ in days)					ICCF
	2	3	4	5	6	
$V-J$	$31.1^{+16.5}_{-15.0}$	$28.6^{+15.4}_{-13.8}$	$28.0^{+15.1}_{-12.2}$	$27.6^{+13.7}_{-12.2}$	$27.3^{+15.1}_{-12.0}$	$20.7^{+13.5}_{-11.0}$
$V-H$	$33.9^{+17.4}_{-14.8}$	$32.0^{+15.4}_{-13.6}$	$32.8^{+15.7}_{-14.0}$	$30.9^{+14.1}_{-12.2}$	$31.9^{+13.6}_{-12.6}$	$25.1^{+12.4}_{-11.0}$
$V-Ks$	$39.2^{+14.9}_{-12.3}$	$37.6^{+13.1}_{-11.1}$	$36.7^{+12.9}_{-10.7}$	$35.2^{+12.3}_{-9.8}$	$36.3^{+12.1}_{-10.7}$	$30.2^{+9.0}_{-7.9}$

5.4.4 Discussion

1. Infrared lag and central luminosity correlation

   The inner radius of the dusty torus in H0507+164 was found to be 0.029 pc using the rest frame time lag between V and K_s-bands. Similar DRM measurements of the size of the dust torus in about two dozen AGN are available in the literature (see Koshida et al. (2014), and the references therein) which are shown in Fig. 8 as empty circles in the lag−luminosity plot. The location of the source H0507+164 indicated by a filled circle is also shown in the same figure. The best-fitted regression line obtained by Koshida et al. (2014) as $\log\tau = -2.11 - 0.2\mathrm{M_V}$, based on a systematic and homogeneous analysis of DRM data of 17 Seyfert 1 galaxies, is shown by a dashed line. Our lag measurement of H0507+164 is in excellent agreement with the lag expected for its luminosity and closely follows the dust lag-optical luminosity correlation of $\tau_{dust} \propto \mathrm{L}^{0.5}$.

2. Structure of the BLR and the dust torus

   From the spectroscopic RM observations of H0507+164, Stalin et al. (2011) estimated the BLR size for this object of $3.01^{+0.42}_{-1.84}$ days in the rest frame based on lag between the optical/UV continuum and the Hβ line emission. The BLR lag is found to be smaller than the dust-lag (lag between V band and K_s band) obtained from this work, as expected from the unified scheme of AGN. Though there are indications of a wavelength dependent lag in our multiwavelength data reported here, they are not statistically significant due to the large errors in their lags. Koshida et al. (2014) found about four to five times larger dust reverberation radius than their BLR radius, and typically a factor 2 smaller than their interferometric radius from an analysis of a sample of 17 Seyfert galaxies. Similarly, the BLR radius measured from RM is found to be smaller than the same observed by NIR interferometry (see Petrov et al., 2012). Such

Centre for Research, CHRIST (Deemed to be University)

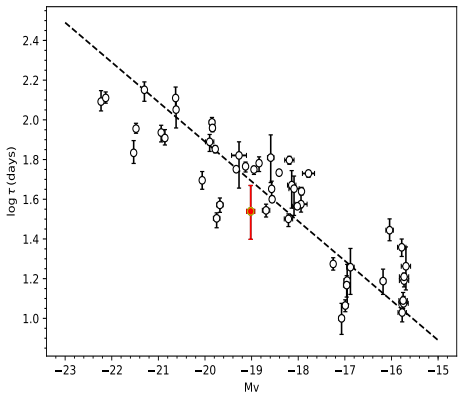

Figure 8: Dust lag−luminosity plot where the empty circles represent the measurements from Koshida et al. (2014) and the filled circle corresponds to the lag between the V and K_s bands determined for H0507+164, which lies close to the regression line (dashed line), obtained by Koshida et al. (2014). The lag times were corrected for the time dilation effect using the redshift of the object.

difference is expected as the radius obtained from RM observations, is a response weighted radius originating from the compact region, while the interferometric radius is flux weighted sensitive to the flux coming from the outer region (Kishimoto et al., 2007). However, there are a few exceptions. For the source Mrk 335 (Du et al., 2014), NGC 4151 (Bentz et al., 2006), and NGC 4593 (Barth et al., 2013), the dust radius (Koshida et al., 2014) is found to be about 10 times larger than the BLR radius. Such varied differences between the mean dust radius and BLR radius known in AGN will hint for variable dust emission (Koshida et al., 2014; Schnülle et al., 2015). To establish this, we need more precise measurements of dust radius for a large sample of AGN. Our ongoing multi-band DRM project on a larger sample will help to understand dust geometry.

5.5 Z229−15

5.5.1 Data Reduction

The optical data was reduced using IRAF and MIDAS following the standard procedures for image reduction, such as bias & dark subtraction and flat-fielding. Cosmic rays were removed using MIDAS. For optical data we adopted aperture photometry based on the growth curve method discussed in Section 4.3.1.

The NIR images were reduced using TIRSPEC NIR Data Reduction Pipeline (Ninan et al., 2014)

Centre for Research, CHRIST (Deemed to be University)

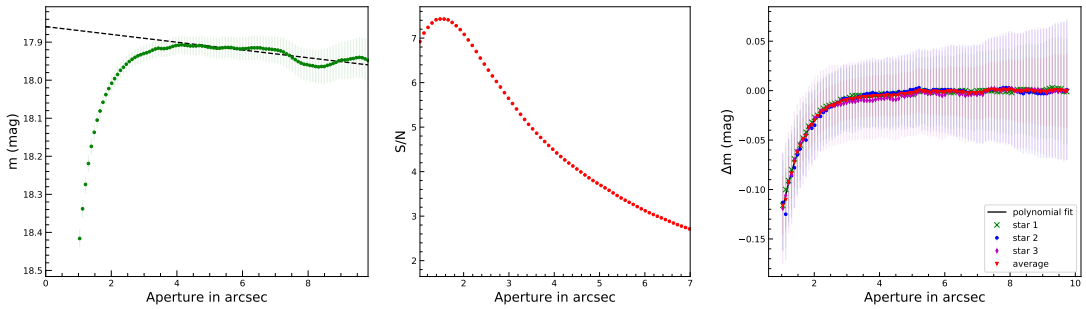

Figure 9: Growth curves for the comparison star in K-band for Z229−15 (left). The dashed black lines represent the best fit lines corresponding to the points with aperture size more than 3 times the FWHM in each band. S/N Vs. aperture curve (middle). Differential magnitude between successive apertures Vs. aperture size plot (right). The green, blue, purple and the red points represent differential magnitudes for comparison star 1, star 2, star 3 and average of those, respectively. The black solid line is the best polynomial fit curve for the average differential magnitudes.

for J, H, K_s bands. The pipeline produce final combined images after subtracting the dark obtained for the same exposure time as the science exposures and flat fielding using twilight flats. But for NIR data as the S/N is very poor compared to optical data, the curve of growth is not perfectly linear at large aperture as shown in Fig. 9 (left) and thus fail to give the optimum aperture. The PSF is also found to change over the CCD frame. So, first we found the aperture size corresponding to maximum S/N (see Fig. 9, middle panel) for each epoch for one comparison star with best S/N, instrumental magnitudes were then obtained at those apertures with maximum S/N for both the comparison star and the target. The aperture size with maximum S/N is found to be smaller than FWHM at individual epoch. We therefore, added a correction factor by taking the difference between magnitudes at apertures corresponding to maximum S/N and FWHM to compensate the light-loss to the obtained instrumental magnitudes. The correction factor was determined from the average differential growth curve which was obtained by plotting instrumental magnitude difference between successive concentric apertures centered on the point sources for three comparison stars present in the same FoV (see right panel of Fig. 9).

The approach adopted for the NIR photometry could not be used for the optical images because of prominent host galaxy contribution. Therefore to get the optical light curves of the AGN, optical magnitudes were first derived using the curve of growth method. The magnitude thus obtained has contribution both from the AGN and the host galaxy. To obtain the magnitude of the AGN, the host galaxy contribution was subtracted by following the procedure given below.

Centre for Research, CHRIST (Deemed to be University)

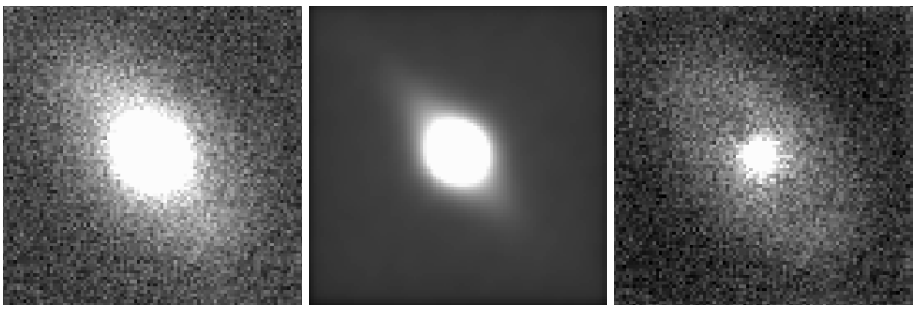

Figure 10: Observed V-band image of Z229−15 (left). Modeled galaxy image (middle) and residual image containing the AGN at the center (right) obtained from GALFIT.

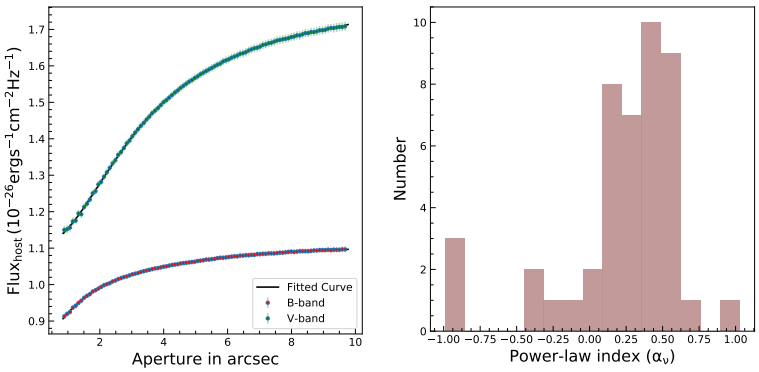

Figure 11: (Left) Host-galaxy flux as a function of aperture size. The points with error bars are the galaxy-flux values and the solid black lines are the best polynomial fits. (Right) Distribution of the spectral index α_v.

5.5.2 Host-galaxy contribution removal

Both optical B and V-band data have prominent host-galaxy contribution to the AGN flux, see Fig. 10 (left) for V-band data. We used GALFIT to the observed B and V-band images for a particular epoch. We used the Sérsic profile and the Edge-on-disk profile to model the underlying galaxy. We generated PSF image from the same FOV. The modeled galaxy image and the residual image that contains the AGN for V-band are shown in Fig. 10 (middle) and (right), respectively.

Aperture photometry was applied on the modeled galaxy image at different concentric aperture sizes and a plot of the obtained galaxy-fluxes with aperture is shown in Fig. 11 (left), where the black solid lines represent the best-fit curves for both B and V-bands. We obtained the host-galaxy fluxes from the best-fit curve at the same size of aperture used at individual epoch as mentioned in Section 4.6.1 in both B and V-band data. Then the optical B and V-band fluxes are corrected for the host-galaxy contribution by subtracting the host-galaxy fluxes from the observed total fluxes in those filters.

Centre for Research, CHRIST (Deemed to be University)

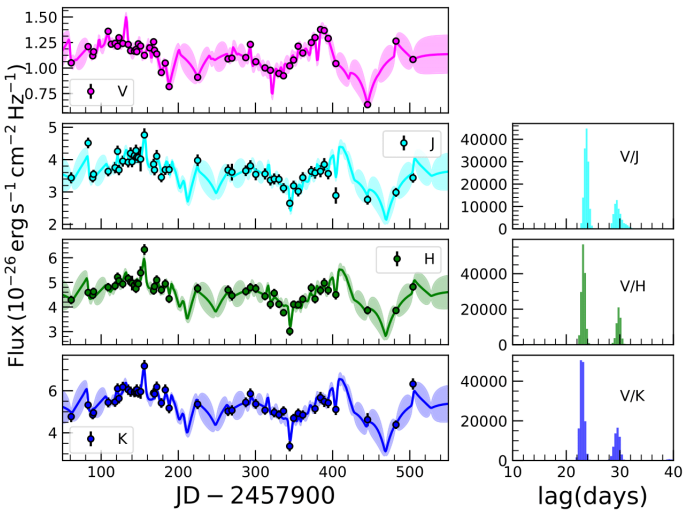

Figure 12: (Left) Light curves in V, J, H, K_s -bands. Points with error-bars represent observed light curves, where as the solid lines with shade are the recovered light curves using JAVELIN. (Right) CCCD obtained from JAVELIN.

5.5.3 Correction for the accretion disc contamination to the NIR flux

As the observed NIR images contain flux contribution both from dust torus and accretion disc, the accretion disc component of the NIR flux needs to be removed from the observed flux to get the NIR flux coming from the torus. We used Equation 4 to find the accretion disc component of the NIR flux for J, H, K_s-bands.

AGN are known to show spectral variability with a bluer-when-brighter behaviour (Meusinger et al., 2011). Therefore, a time dependent α_ν needs to be used to correct for the contribution of the accretion disc emission to the NIR flux. α_ν can be estimated from the simultaneous observations between two optical bands such as B and V-bands following Mandal et al. (2019) and is given by

$$\alpha_\nu = \frac{\ln(f_B/f_V)}{\ln(\nu_B/\nu_V)} \tag{5}$$

The observations in the optical and each of the NIR bands typically differ by less than 300s at any given epoch, and therefore, they were considered as simultaneous observations while removing the contribution of accretion disc to each of the NIR bands. First, we obtained α_ν from the simultaneous observations between the optical B and V-bands. The distribution of α_ν thus obtained is shown in Fig. 11 (right). The median value of α_ν is 0.32 with a standard deviation of 0.42 determined from the distribution of α_ν. Then we calculated $f_{NIR,disc}$ using our obtained α_ν. There are only few epochs for which we do not have simultaneous optical and NIR observations, for those epochs we used the

Centre for Research, CHRIST (Deemed to be University)

Table 5: Variability statistics in BVJHK_s bands in observer's frame where $\lambda_{\rm eff}$ is the effective wavelength in Angstroms. The average values ($< f >$) and the standard deviation σ of the BVJHK_s light curves are in units of $10^{-26}\,{\rm erg\,s^{-1}\,cm^{-2}\,Hz^{-1}}$.

Filter	λ_{eff}	$< f >$	σ	F_{var}	R_{max}
B	4363	1.25	0.21	$0.171 \pm < 0.001$	2.562
V	5448	1.14	0.14	$0.127 \pm < 0.001$	2.148
J	12200	3.66	0.43	0.106 ± 0.002	1.797
H	16300	4.64	0.50	0.100 ± 0.002	2.101
K_s	21900	5.46	0.61	0.102 ± 0.002	1.905

median value of α_v to calculate $f_{\rm NIR,disc}$. Finally, the contribution of the accretion disc evaluated using Equation 4 was subtracted from the observed NIR fluxes. After getting the final fluxes we generated optical and NIR light curves for further analysis. The errors in the final flux values in different bands were obtained using the method of propagation of errors during the various steps of flux determination.

We separately subtracted the accretion disk component of the NIR fluxes from the observed fluxes for a constant value of $\alpha_v = 0.1$ as suggested by Yoshii et al. (2014) and Minezaki et al. (2019) for J, H. K_s-bands.

5.5.4 Analysis, Results and Discussion

1. Fig. 12 (left) shows the light curves of Z229−15 in optical V- bands and three NIR J, H, K_s- bands. The NIR light curves were corrected for the accretion disc contamination. There is negligible contamination from the radio jet to the observed flux variations as the source is radio-quiet. The variability statistics of the light curves are mentioned in Table 5.

2. CCF analysis to find the lag

   We used two well-known methods, namely ICCF (Gaskell & Sparke, 1986; Gaskell & Peterson, 1987) and DCF (Edelson & Krolik, 1988) to find the time lag between the optical (B and V) and different NIR (J, H, K_s) bands. We also used the JAVELIN code developed by Zu et al. (2011) to estimate the lag between different optical and NIR light curves by modelling the light curves using DRW model from the observed light curves. Fig. 12 (right) represents the CCCD obtained using JAVELIN between V and J (top), V and H (middle), V and K_s (bottom),

Centre for Research, CHRIST (Deemed to be University)

Table 6: Median values of time delays with errors in days as obtained from the centroids of DCF and ICCF, from CCF peak and JAVELIN in the observer's frame.

Band	DCF	ICCF	CCF Peak	JAVELIN
		varying α		
V − B	$0.63^{+4.73}_{-4.35}$	$0.10^{+2.72}_{-2.00}$	$0.00^{+2.00}_{-0.00}$	$0.58^{+0.16}_{-1.16}$
V − J	$24.89^{+14.74}_{-17.01}$	$13.12^{+12.27}_{-11.00}$	$12.00^{+12.89}_{-11.12}$	$23.98^{+5.53}_{-0.52}$
V − H	$19.67^{+17.28}_{-10.99}$	$16.11^{+5.84}_{-5.97}$	$14.00^{+7.89}_{-8.11}$	$23.37^{+6.37}_{-0.45}$
V − K_s	$28.42^{+11.39}_{-16.94}$	$21.85^{+6.09}_{-5.95}$	$22.00^{+8.15}_{-9.85}$	$23.17^{+6.28}_{-0.49}$
		constant $\alpha = 0.1$		
V − J	$36.45^{+12.16}_{-15.65}$	$29.85^{+7.07}_{-8.84}$	$30.00^{+8.15}_{-9.85}$	$28.17^{+1.82}_{-1.66}$
V − H	$31.49^{+9.81}_{-12.10}$	$26.82^{+6.91}_{-5.71}$	$28.00^{+5.18}_{-4.82}$	$25.10^{+2.75}_{-0.78}$
V − K_s	$37.01^{+7.13}_{-12.82}$	$31.84^{+6.09}_{-5.39}$	$32.00^{+8.16}_{-5.84}$	$24.422^{+2.91}_{-0.80}$

respectively. The obtained time lags between different optical bands and NIR bands are given in Table 6.

3. Infrared lag and optical luminosity correlation

We found the inner radius of the dust torus of Z229−15 as 0.018 pc based on the lag between V and K_s-bands. There are more than 40 sources including Seyfert galaxies at low redshift (Suganuma et al., 2006; Koshida et al., 2014) as well as quasars at high redshift (Minezaki et al., 2019) for which the DRM was applied to measure the inner radius of the dust torus. Minezaki et al. (2019) used a constant spectral index α = 0.1 to remove the accretion disc contamination in the observed K-band flux and found a dust radius−optical luminosity ($r_{dust} - \lambda L_\lambda(V)$) correlation with no break using their target quasars and Seyfert galaxies from Koshida et al. (2014) as given by:

$$\log r\,(\mathrm{pc}) = -1.021 \pm 0.023 + (0.424 \pm 0.026)\log\Big(\frac{L_V}{10^{43.7}\,\mathrm{erg\,s^{-1}}}\Big) \tag{6}$$

The empty and filled black circles in Fig. 13 represent the objects from Minezaki et al. (2019) and Koshida et al. (2014), respectively, the blue triangle point represents H0507+164 (Mandal et al., 2019), the green square and circle correspond to Z229−15 for constant α = 0.1 and observed time dependent α_v, respectively. In the same plot we show the best regression line as obtained by Minezaki et al. (2019) by dashed black line and given by Equation 6. We see

Centre for Research, CHRIST (Deemed to be University)

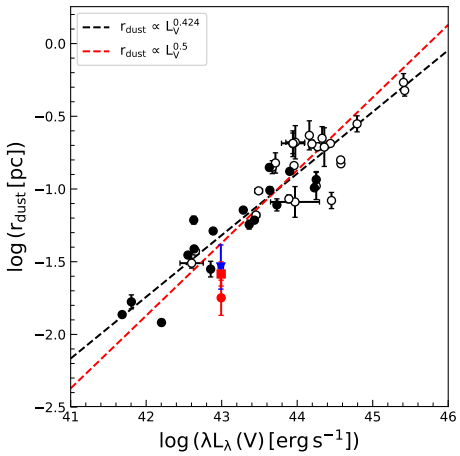

Figure 13: Lag-luminosity plot. The empty and filled black circles are the objects from Minezaki et al. (2019) and Koshida et al. (2014), respectively, triangular blue point represents H0507+164 obtained by Mandal et al. (2019), the green square and circle correspond to obtained measurements for Z229−15 for $\alpha = 0.1$ and observed α, respectively obtained in this work.

that our lag obtained using observed spectral index α_ν is quite smaller and deviates from the best-fit line. Similar kind of shortened Hβ lags compared to traditional $R_{BLR} - L$ relation were known from the studies of BLR reverberation mapping over wide range of luminosities and redshifts from the campaign of Reverberation mapping on super-Eddington accreting massive black holes (SEAMBHs) by Du et al. (2018) and SDSS-RM project carried out by Shen et al. (2015); Grier et al. (2017b). According to Du et al. (2018) the self-shadowing effects of slim accretion discs causes shrinking of the BLR ionization front, which results in shortened Hβ lag with increasing accretion rate as seen in SEAMBHs. Similarly, the shortened Hβ lags observed in low accreting mass AGN are due to retrograde accretion onto the black holes where black hole spin plays an important role. So based on these study from BLR reverberation we can not rule out the possibility of the effect of accretion rate on the torus size as well. On the other hand if we use a constant $\alpha = 0.1$, as suggested by Minezaki et al. (2019) to get accretion disc component corrected NIR fluxes, we obtain larger radius of the torus size of $30.99^{+5.93}_{-5.25}$ days equivalent to 0.026 pc based on the lag between V and K_s -bands. This lies close to the best fit line corresponding to $r_{dust} \propto L_V^{0.424}$ in the lag-luminosity plot and consistent with the results obtained by Minezaki et al. (2019).

Thus there is a large discrepancy between the results obtained from the observed α_ν that varies with time and a constant $\alpha = 0.1$ as used in the previous studies. This discrepancy raises a

Centre for Research, CHRIST (Deemed to be University)

question on the validity of using a constant spectral index α_v in DRM studies.

4. Structure of the BLR and the dust torus

From spectroscopic monitoring of Z229−15, Barth et al. (2011) obtained a BLR size of $3.86^{0.69}_{-0.90}$ days. And, according to Koshida et al. (2014) the inner edge of the torus is about 5 times larger than the size of the BLR. Our derived dust lag is also about 5.5 times larger than the BLR lag of the source. This agrees with that of Koshida et al. (2014) and suggests that the BLR lies well inside the dust torus as expected from the Unification scheme of AGN. Though there is a hint of a wavelength dependent lag in our multiwavelength studies as previously obtained by Mandal et al. (2018), considering the large errors we conclude that they are consistent with each other.

5.6 Estimation of the size and structure of the broad line region using Bayesian approach

We constrained the geometry and other characteristics of AGN by modelling their continuum and line light curves, using a Bayesian approach.

5.6.1 Analysis

1. Variability

The line and continuum variability of our sample of sources was characterized by using the F_{var} parameter (Vaughan et al., 2003) as described in Section 4.3.5 including the values of R, the ratio between the maximum and minimum fluxes in the light curves.

2. Reconstruction of Light Curve

The PBMAP code developed by Li et al. (2013) was used to carry out the light curve modelling. Using the damped random walk model (DRW; Kelly et al. 2009) the code reconstructs the continuum light curve from the the irregularly sampled observed continuum light curve following a Bayesian approach. It then reconstructs the line light curve by considering (a) the point like central source ionizes the BLR isotropically (b) the BLR is an axisymmetric disk like structure that consists of a large number of point-like discrete clouds of equal density and that re-radiates the UV/optical continuum as emission lines and (c) the BLR is viewed at an inclination angle denoted by θ_{inc} and subtended by a solid angle defined by the opening angle (θ_{opn}). The disk-like structure of BLR assumed in this model is depicted in Fig. 14.

Centre for Research, CHRIST (Deemed to be University)

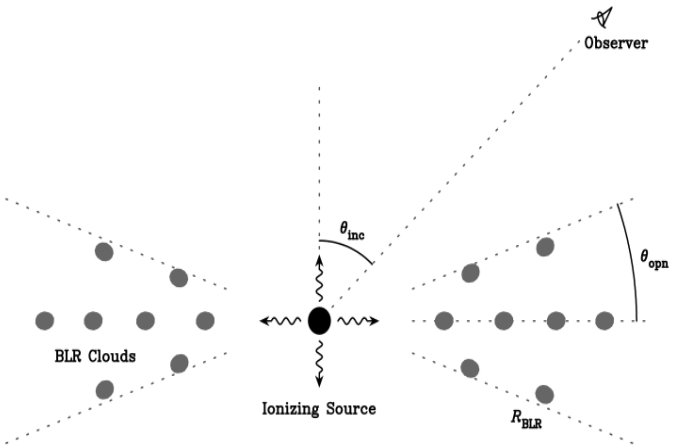

Figure 14: A diagram of the BLR chracterized by a flexible disk-like geometry with an inclination angle θ_{inc} to the observer along the line of site and an opening angle θ_{opn} (Li et al., 2013) . A point like central ionizing source producing isotropic UV/optical emission illuminates the surrounding BLR clouds.

5.6.2 Results and discussion

1. Flux Variability

   Fig. 15 represents the distribution of the amplitude of variability, F_{var} for both the continuum and line that includes MgII, Hβ and Hα. We applied a two sample, Kolmogorov-Smirnov test on the distributions and found that the two distributions are indeed different with a statistic of 0.317 and a p value of 4.0×10^{-4}. The mean F_{var} values for continuum and line are 0.057 and 0.106, respectively with errors lesser than 0.001. While separating the sample into different lines, we found mean F_{var} values of 0.065 and 0.119 for continuum and line, respectively for Hβ. Similarly, for Hα, the mean F_{var} values for continuum and line are 0.041 and 0.076, while for MgII we found mean F_{var} of 0.057 and 0.120 for continuum and line, respectively. The F_{var} in line is thus found to exceed that of the continuum. Such increased variations in emission lines relative to continuum support the deviation of BLR from the linear response to the ionizing continuum (Rashed et al., 2015; Li et al., 2013).

2. BLR characteristics

   Pancoast et al. (2011) developed a model based on Bayesian approach to constrain the structure and kinematics of BLR and subsequently was applied to Arp 151 (Brewer et al., 2011) and Mrk 50 (Pancoast et al., 2012). In addition to Mrk 50 and Arp 151, more AGN were studied for BLR modelling (Li et al., 2013; Pancoast et al., 2014; Grier et al., 2017a; Williams et al., 2018). In

Centre for Research, CHRIST (Deemed to be University)

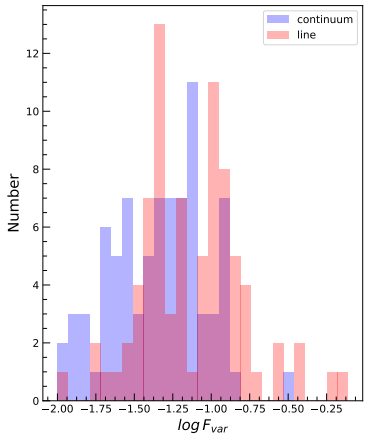

Figure 15: Distribution of excess variance of the line and continuum light curves.

this work we used the BLR modelling based on Li et al. (2013), which is an independent implementation of the approach of Pancoast et al. (2011), with the additional inclusion of (a) non-linear response of emission lines to the continuum variations and (b) option to carry out a detrending of the light curves. Here, we analysed the data for 58 objects with 83 independent measurements for Hβ,Hα and MgII lines, which is double the number of AGN studied earlier (Li et al., 2013) for uncovering the characteristics of BLR.

Few examples to illustrate our BLR model fits to their observed continuum and line reverberation data are shown in Fig. 16. In these plots the data points with error bars represent the observed light curves and the thick solid lines are the reconstructed light curves by the model.

The transfer functions are found to have different shapes. For example in J1412+534 (top left panel; α_{2000} = 14:12:14.20, δ_{2000} = 53:25:46.7), the transfer function has single peak at $\tau = \tau_{lag}$ with θ_{inc} = 4.0 $\pm$ 2.8 deg and θ_{opn} = 6.0 $\pm$ 3.9 deg obtained from the model. The transfer function for J1407+537 (bottom left; α_{2000} = 14:07:59.07, δ_{2000} = 53:47:59.8) is double peaked with θ_{inc} = 65.0 $\pm$ 22.1 deg and θ_{opn} = 37.0 $\pm$ 26.5 deg. For J1417+517 (bottom right; α_{2000} = 14:17:06.68, δ_{2000} = 51:43:40.1), the transfer function shows a top hat structure with derived θ_{inc} and θ_{opn} of 57.9 $\pm$ 21.6 deg and 51.8 $\pm$ 25.8 deg, respectively. The peak of the transfer function can only be used as an indication of the size of the BLR for objects that show a single peaked transfer function. We found a) for a thick disc, larger $\theta_{\rm inc}$ tends to produce a double-peaked transfer function, as seen in the case of object J1407+537 (bottom left of Fig. 16) with $\theta_{\rm inc}$ = 65.0 $\pm$ 22.1 deg. As $\theta_{\rm inc}$ increases, the object appears more edge on and the radiation coming both from the front and back surfaces makes a double peak transfer function where the stronger peak appears closer to the center. b) a larger opening angle $\theta_{\rm opn}$ tends to broaden the

Centre for Research, CIRIST (Deemed to be University)

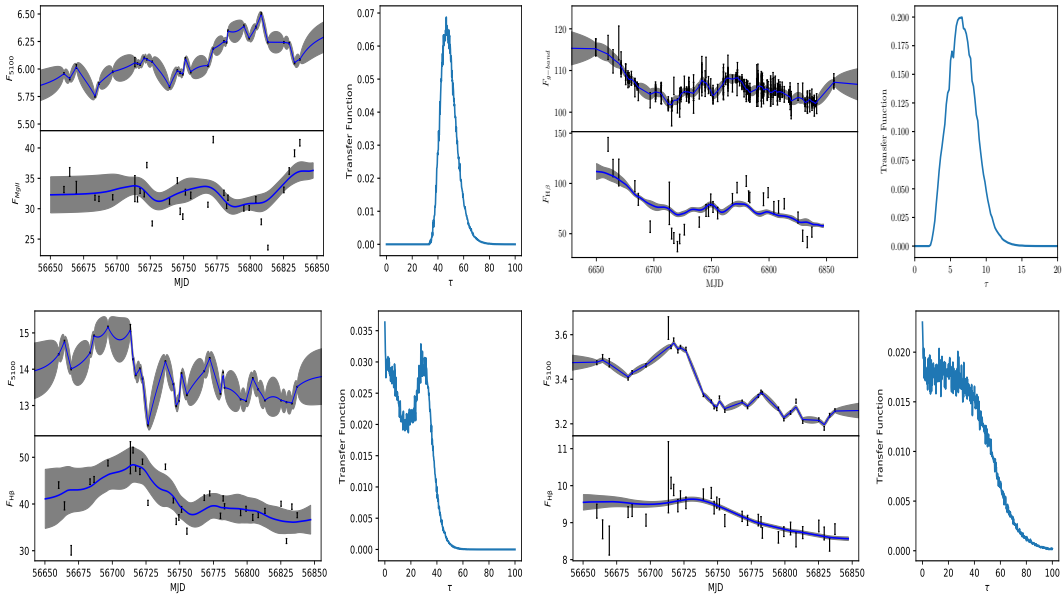

Figure 16: Examples of BLR model fits to four objects J1412+534 (top left), J1421++525 (top right), J1407+537 (bottom left) and J1417+517 (bottom right). For each object, in the left hand panels, the data points with error bars are the observed light curves. The thick solid lines are the reconstructed light curves. The grey shaded areas represent the uncertainties in the reconstructed light curves. The corresponding transfer functions for the objects are shown on the right hand panels.

transfer functions toward top-hat as seen in case of J1417+517 (bottom right of Fig. 16) which has a $\theta_{\rm opn}$ of 51.8 ± 25.8 degree. As $\theta_{\rm opn}$ increases the BLR tends to a spherical geometry and the virial motion of the clouds contribute to the transfer function making the transfer function broaden towards a top-hat structure.

3. Relation between $R^{\rm mod}_{\rm BLR}$ and $R^{\rm CCF}_{\rm BLR}$

   The comparison of the BLR size derived by the modelling approach ($R^{\rm mod}_{\rm BLR}$) with that obtained using the traditional CCF analysis ($R^{\rm CCF}_{\rm BLR}$) is illustrated in Fig. 17. Our obtained model BLR size is in general consistent with that derived from CCF, however, with a large scatter. The mean of the ratio between the size of the BLR estimated by modelling and CCF is 1.29 with standard deviation of 1.24.

4. BLR size luminosity relation

   We estimated $R_{\rm BLR}$ from modelling of the sources using different lines of Hβ, Hα and Mg II. The derived $R_{\rm BLR}$ as a function of luminosity for Hβ line is shown in Fig. 18 (left). We found

Centre for Research, CHRIST (Deemed to be University)

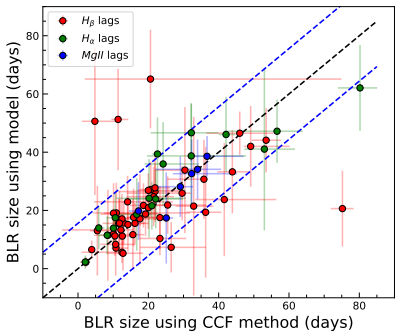

Figure 17: Comparison of the BLR size obtained in this work from the model and that from CCF analysis taken from literature. Red colored circles correspond to Hβ lags, whereas green and blue circles correspond to Hα and Mg II lags respectively. The black dashed line shows y=x, while the blue dashed lines are y = x $\pm$ σ, where σ = 15.59 days is the standard deviation of the BLR sizes obtained from CCF analysis.

the following relation using weighted linear least squares fit

$$\log\left(\frac{R_{\rm BLR(H\beta)}}{1\rm day}\right) = \beta + \alpha\log(\lambda L_\lambda) \tag{7}$$

with α = 0.58 $\pm$ 0.03 and β = -24.08 $\pm$ 1.13. λL_λ is estimated at λ = 5100 Å. Our α and β are similar to the values of $\alpha = 0.519^{+0.063}_{-0.066}$ and $\beta = -21.3^{+2.9}_{-2.8}$ obtained by Bentz et al. (2009) with $R_{\rm BLR}$ measured from CCF analysis of the observed continuum and line light curves. Li et al. (2013) using the approach adopted in this work for 40 quasars with $H\beta$ measurements found a value of α = 0.55 $\pm$ 0.03, which is in agreement with the one found by us using a different sample of 51 AGN as well as their sample for Hβ line.

Similarly the relation between R_{BLR} and L_{5100} for objects with $H\alpha$ measurements is shown in Fig. 18 (middle). Using weighted linear least squares fit to the data we found

$$\log\left(\frac{R_{\rm BLR(H\alpha)}}{1\rm day}\right) = \beta + \alpha\log(\lambda L_\lambda) \tag{8}$$

with $\alpha = 0.19 \pm 0.12$ and $\beta = -6.86 \pm 5.16$ as shown by the dashed blue line. Using unweighted linear least squares fit to the data as shown by dashed red line, we found

$$\log\left(\frac{R_{\rm BLR(H\alpha)}}{1\rm day}\right) = \beta + \alpha\log(\lambda L_\lambda) \tag{9}$$

with $\alpha = 0.47 \pm 0.08$ and $\beta = -19.10 \pm 3.67$ which closely matches with α=0.5 based on simple photoionization arguments.

Centre for Research, CUSAT (Deemed to be University)

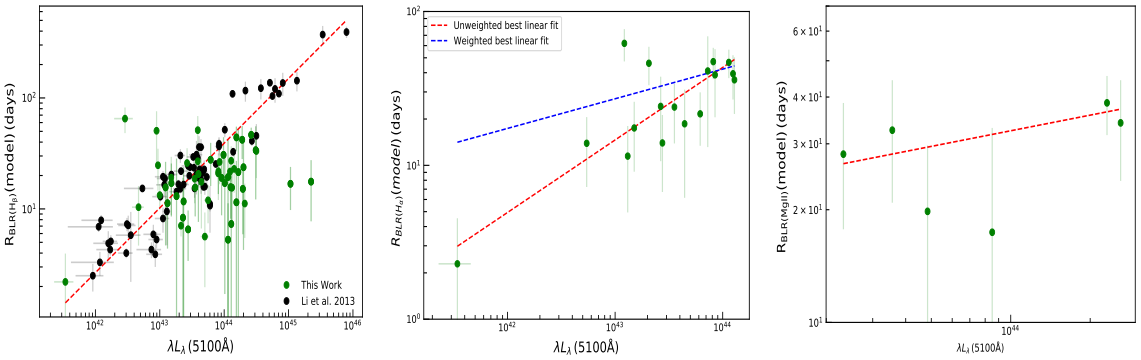

Figure 18: Relation between the radius of the BLR obtained from the model for sources with Hβ (left), Hα (middle) and Mg II (right) line light curves and their continuum luminosity at 5100 Å. Here, filled green circles are the objects studied in this work, while the filled black circles are the objects from Li et al. (2013). The dashed red line is the best fit to the data points.

We have only six objects with Mg II line light curves. The relation between $R_{\rm BLR}$ and L_{5100} for sources with Mg II lin light curve is given in Fig. 18 (right). We plotted the data with the form

$$\log\left(\frac{R_{\rm BLR(MgII)}}{1\,\rm day}\right) = \beta + \alpha\log(\lambda L_\lambda) \tag{10}$$

and we found $\alpha = 0.14 \pm 0.08$ and $\beta = -4.59 \pm 3.58$.

The relation between R_{BLR} and luminosity of MgII and Hα deviate from the value expected from photoionization argument. This is only due to the poor quality of measurement available on small number of sources. R_{BLR} measurements on large number of objects are needed to firmly establish the relationship between R_{BLR} and luminosity determined from Mg II and Hα emission lines.

5. The Virial factor $f_{\rm BLR}$

The Virial factor $f_{\rm BLR}$ used to estimate black hole (BH) mass as given in Equation 1 depends on the kinematics, geometry and inclination of BLR. One of the many factors provided by the Bayesian based modelling approach carried out here is the capability to estimate $f_{\rm BLR}$. For a disc like BLR, (see Collin et al., 2006; Li et al., 2013; Rakshit et al., 2015) $f_{\rm BLR}$ can be written as

$$f_{\rm BLR} \approx (\sin^2\theta_{\rm opn} + \sin^2\theta_{\rm inc})^{-1} \tag{11}$$

Centre for Research, CHRIST (Deemed to be University)

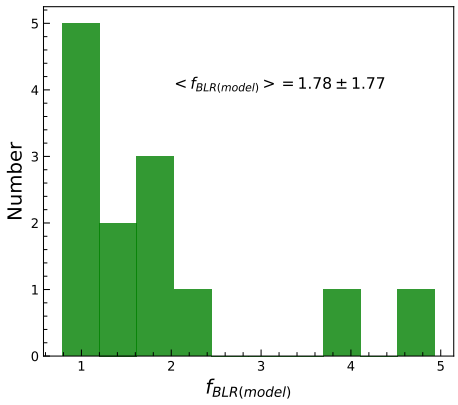

Figure 19: Distribution of the virial factor $f_{\rm BLR}$ obtained for the objects analysed in this work

where $\theta_{\rm inc}$ and $\theta_{\rm opn}$ are the inclination angle and opening angle of the disc, respectively. Following Li et al. (2013) we calculated $f_{\rm BLR}$ for only those objects with $\theta_{opn} < 40^{\circ}$. Our obtained values of $f_{\rm BLR}$ range from 0.79 to 4.94, with a mean value of 1.78 ± 1.77. A distribution of $f_{\rm BLR}$ is shown in Fig. 19.

5.7 Finding quasars in the ILMT stripe

An ideal way to select quasars for reverberation mapping observations is to find quasars that are variable. An upcoming survey such as the ILMT will be able to observe a stripe of the sky with a cadence of about 3 days in each of the g', r', i' bands. Such a data set will help one to select quasars for reverberation observations. An alternate way is to identify known quasars from already existing surveys that will be covered by ILMT. Such a quasar catalogue can also serve as astrometric calibrators to bring the ILMT observations from the pixels co-ordinate system to the world co-ordinate (α, δ) system.

5.7.1 Methods followed and the resulting catalogue

Quasars represent quasi-ideal astrometric reference sources with negligible proper motion PM and parallaxes and are thus suitable for use to carry out astrometric calibration (Souchay et al., 2015) of the ILMT survey. We therefore retrieved accurate position, PM and trigonometric parallax for all quasars available in the Milliquas catalogue cross-correlated with the *Gaia*-DR2 database in order to select a sub-set of them for the ILMT use as *Gaia*, operated by the European Space Agency provides precise positions of celestial sources with milli-arcsec accuracy. The absolute or resultant PM μ is

Centre for Research, CHRIST (Deemed to be University)

given by

$$\mu = (\mu_\alpha^2 cos^2\delta + \mu_\delta^2)^{1/2} \tag{12}$$

where α and δ represent the right ascension (RA) and declination (DEC), respectively. The values of $\mu_\alpha cos\delta$ and μ_δ were collected from the *Gaia*-DR2 database and the error in μ was calculated using the standard error propagation method. We followed the following steps to arrive at a separate list of quasars in the ILMT stripe.

1. The nearly 2 million candidates in the Milliquas catalogue were cross-correlated with *Gaia*-DR2 with angular separation of less than 2". This leads to a sample of 1235600 objects spanning a range of redshifts up to z = 6.4.

2. *Gaia*-DR2 provides two parameters relevant for quasar target selection, such as astrometric excess noise (ε_i) and its significance namely the astrometric excess noise significance (D). Excess noise ε_i represents the discrepancy between the observations and the best-fitting standard astrometric model adopted by *Gaia* and the significance of ε_i is given by its significance namely D (Lindegren et al., 2012). If, D $\leq$ 2 quantifies that ε_i is probably not significant and the source may be astrometrically well-behaved even if ε_i is large[4]. Hence, we selected only sources with D $\leq$ 2 from *Gaia*-DR2. We found a total of 1047747 quasars covering the whole sky. Fig. 20 (left) represents their PM distribution which clearly shows that most of them have PM less than 20 $mas\ yr^{-1}$ except for a few objects (about 0.25%) with a mean value and standard deviation of 1.808 $mas\,yr^{-1}$ and 2.878 $mas\,yr^{-1}$, respectively.

3. To arrive at a separate catalogue of quasars in the ILMT stripe, first we calculated the extra width of the ILMT stripe to consider the effect of precession and found that if we take a stripe of width $\sim 34'$ instead of $\sim 27'$, the effect of precession during the next 10 years will be taken into account as shown in Fig. 20 (right). So, only those quasars were selected having a declination (δ) in the range $29.09^\circ \leq \delta \leq 29.66^\circ$ and G-mag $\leq$ 21 from the sample of 1047747 quasars obtained from step 2 accessible for observations with the ILMT. This yielded a sample of 6904 quasars. We do not have the redshift information for slightly less than 2% of these, in the Milliquas catalogue. Excluding those, we arrived at a final final sample of 6755 quasars available within the ILMT stripe.

[4]https://gea.esac.esa.int/archive/documentation/GDR2/Gaia_archive/chap_datamodel/sec_dm_main_tables/ssec_dm_gaia_source.html

Centre for Research, CHRIST (Deemed to be University)

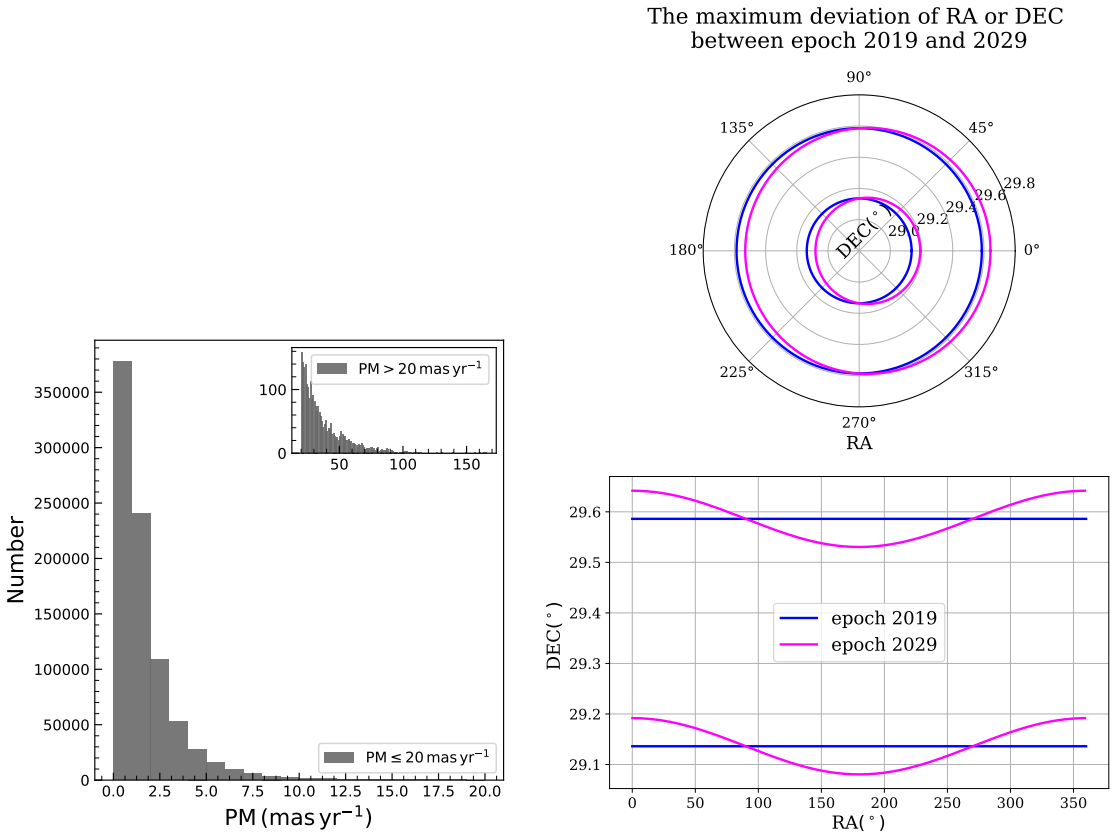

Figure 20: Left panel: Distribution of the PM for quasars in the Million Quasars catalogue with D ≤ 2. PM distribution of the quasars with PM > 20 $mas\,yr^{-1}$ is shown in the small box on the same figure. Right panel: (Top) Polar plot showing the astrometric deviation of the ILMT stripe between the 2019 and 2029 epochs due to precession. (Bottom) Deviation in astrometry between the 2019 and 2029 epochs considering that the original ILMT stripe is rectangular in 2019 (blue lines) and pink lines represent the same in 2029.

4. We only found 17 candidates in the ILMT stripe with PM > 20 $mas\,yr^{-1}$ and all of them are fainter than 19.5 mag in the G-band. As the nature of these 17 sources was difficult to establish because of the lack of optical spectra for them, we neglected those 17 quasars from our list. We finally arrived at a sample of 6738 quasars that will be visible with the ILMT and could be used as astrometric calibrators.

5.7.2 Applications of the catalogue

1. Astrometric calibration of the ILMT field

   The main use of this catalogue of quasars will be to calibrate the ILMT observations in the world coordinate system. In order to estimate the astrometric accuracy for the survey we performed

Centre for Research, CIRIST (Cochin University)

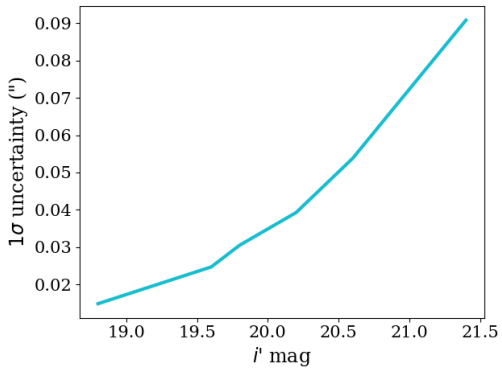

Figure 21: Estimation of the 1σ uncertainty in the astrometric position of point sources with different magnitudes in the ILMT CCD images.

a Monte Carlo simulation by generating several synthetic CCD frames having a circular Gaussian point spread function at random locations corresponding to different SDSS i' magnitudes assuming a single scan (i.e. exposure time of 102 seconds) as demonstrated by Kumar et al. (2018) given the pixel scale of 0.4" and median seeing at Devasthal observatory of 1.1" (Sagar et al. 2000; Sagar, Kumar & Omar 2019 and references therein). We used the Source Extractor software developed by Barbary (2016) to estimate the centroid of each synthetic source and the 1σ accuracy in estimating the centroid of a point source having a limiting i' magnitude of 21.4 mag with the 4-m ILMT was found to be 0.09" (see Fig. 21).

2. Quasar Variability

Quasars are known to vary over diverse time scale since their discovery and their optical flux variations have been studied over a range of time scales from minutes to days (Wagner & Witzel, 1995; Ulrich et al., 1997). But most of the observations are limited by the time resolution manifested as gaps in the data. The 4K×4K CCD camera mounted on the ILMT has three different SDSS equivalent filters g', r' and i' and can operate over the 4000 to 11000 spectral range. Only one of those filters will be used throughout a single night with a typical exposure time for a single frame of $\sim$ 104 s (Surdej et al., 2018). The observing strategy of the ILMT will enable one to collect good quality data for most of the 6738 quasars that we have arrived at in this work primarily for astrometric calibration. Observations in different optical bands can also be used to study their colour variability. New candidate quasars can also be discovered based on colour-colour diagram (Richards et al., 2002) as well as optical variability characteristics (Graham et al., 2016) when more epochs of observations become available from the ILMT in the future. Quasars that are found to be more variable from ILMT observations in the future

Centre for Research, CHRIST (Deemed to be University)

can also be pre-selected for future reverberation mapping program.

3. Variability of lensed quasar

Gravitational lensing, constitutes a powerful tool that finds applications in many astrophysical areas. Gravitational lensing, the effect of deflection of light by a foreground intervening compact object (galaxy, cluster, etc.) of distant quasars leads to the formation of multiply imaged quasars (Ehlers & Schneider, 1992; Narayan & Bartelmann, 1999). It is possible to measure time delays between the lensed quasar images from light curves using CCF analysis to determine the Hubble-Lemaître constant H_0 (Refsdal, 1964). About 24 lensed quasars are studied till now to measure such time delays that range from a few days to a few years (Rathna Kumar et al., 2015). Long term monitoring of lensed quasars is required to measure such time delays. We have only identified one gravitationally lensed quasar in the ILMT stripe, namely J1251+295 (α_{2000} = 12:51:07.57, δ_{2000} = 29:35:40.50) which has 4 lensed images with maximum angular separation of $\sim$ 1.8" and can be easily resolved with the ILMT (the median seeing at Devasthal site is of the order of 1.1"). The ILMT will be able to provide good light curves for this source and many others.

6 Summary and future work

1. Summary

Probing the central regions of AGN via the technique of reverberation mapping is an established technique for more than three decades (Gaskell & Sparke, 1986; Gaskell & Peterson, 1987). Several observational programs carried out in the interim have increased the number of sources with known BLR and dusty torus size. These observational programs led to the acceptance of a general trend between R_{BLR} and the continuum luminosity as well as R_{torus} and the continuum luminosity. Also very recently advancements in observational techniques have lead to the direct imaging of nearby AGN using very long baseline interferometry at the Very Large Telescope, at European Southern Observatory (ESO). In spite of that there is a need to increase the number of sources with measured BLR and dust torus size that covers a range of redshift and luminosity to refine the correlations already known that spans a limited luminosity range. This leads to the present program called REMAP that aims to observe more number of AGN to determine dust torus size and BLR size. Such a program to determine the size of BLR, using Indian observational facilities was undertaken for the first time about a decade ago (Stalin et al., 2011).

Centre for Research, CHRIST (Deemed to be University)

The observational strategy followed in this present study is to carry out good S/N and time sampling observations of more AGN to get BLR as well as the torus size. We summarize the main results this work here and also outline extensions of this project that will be pursued in the future. The major findings of the present study are

(i) We found the inner extent of the dusty torus in two AGN namely H0507+164 and Z229−15 for the first time. We found R_{torus} = 0.029 and 0.018 pc for H0507+164 and Z229−15, respectively. These two new measurements also nicely fit into the R_{torus} − luminosity relation obtained based on the monitoring of about three dozen AGN.

(ii) Using the technique of photometric reverberation we found a lag between the continuum and Hα line to be $21.44^{+0.53}_{-1.95}$ days. This is in agreement with the lag obtained between the continuum and Hβ (lag = $20.7^{+3.5}_{-2.7}$ days) obtained from spectroscopic reverberation. This new measurement also lies on the known R_{BLR} − luminosity plot known from observations of 35 AGN by Bentz et al. (2009).

(iii) By compiling line and continuum light curves from the literature for a sample of 58 AGN, and by following the Markov chain Monte Carlo approach, we were able to determine the structure and other characteristics of BLR.

(iv) As reverberation mapping observations rely on the variability nature of quasars, it is ideal to observe quasars that are known to be variable. The upcoming survey with the ILMT will provide good cadence data which will enable one to pre-select variable quasars for further reverberation monitoring. Towards this we have identified 6738 known quasars that lie in the ILMT stripe. Future ILMT observations will quantify their variability nature. This new quasar catalogue can also serve as astrometric calibrators to bring the ILMT observations in the world co-ordinate system.

2. Future plan

BLR RM program: We have started narrow band photometric monitoring observations for one quasar to find the BLR size and measure M_{BH} from a single epoch spectrum using HCT as a part of our REMAP program. We have future plan to observe more objects spectroscopically as velocity resolved RM progarm using 3.6 m Devasthal Optical Telescope (DOT) to measure M_{BH}.

DRM program: We have total 8 sources in our REMAP DRM program. We obtained results for 2 objects, namely H0507+164 and Z229−15. Monitoring observations for 2 more sources are

Centre for Research, CHRIST (Deemed to be University)

completed. We are thus left with 4 more sources to observe using HCT. This will be pursued in the future.

7 Structure of the Thesis

7.1 Outline of the Thesis

This thesis is mainly motivated to find the extent of BLR and torus in AGN using the technique of reverberation mapping. This details of this work will be presented as seven chapters in the thesis as shown below.

7.1.1 Chapter 1: Introduction

This chapter starts with the basic introduction to AGN, gives a brief overview of the available methods to measure BLR and torus size, discusses the current status in this field, the avenues for new research and ends with the motivation of the present thesis.

7.1.2 Chapter 2: Sample, Observations, Reduction and Analysis

This chapter gives the details of how the sample was selected for the thesis work and the observational strategy adopted. It gives details of the instruments that acquired data used in this thesis. The nature of the data and the various procedures followed to reduce the data is explained in detail in this Chapter. In addition to that, the chapter also provides details of the models used to analyse the available RM data to estimate the size and structure of BLR region. It also details the cross-correlation analysis techniques used in this work to find the correlation between flux variations in different wave-bands.

7.1.3 Chapter 3: BLR Reverberation on Mrk 590, a changing look AGN

This chapter presents the results obtained on the source Mrk 590 using photometric reverberation observations.

7.1.4 Chapter 4: Dust reverberation on H0507+164 and Z229−15

This chapter presents the first time measurements on the inner edge of the dusty torus in two AGN namely, H0507+164 and Z229−15.

Centre for Research, CHRIST (Deemed to be University)

7.1.5 Chapter 5: Estimation of the size and structure of the broad line region using Bayesian approach

The results on the structure of BLR obtained via a Markov chain Monte Carlo approach is presented in this chapter.

7.1.6 Chapter 6: Quasars in ILMT stripe

This chapter presents the selection of known quasars that will be covered by the ILMT in the future. In addition to that it also presents the usability of such a catalogue.

7.1.7 Chapter 7: Summary and Future prospects

This last chapter compiles the outcome of the problems addressed in this thesis along with detailed discussions and conclusions. This chapter also details few research problems that can be pursued in the future.

Centre for Research, CHRIST (Deemed to be University)

Publications and presentations

Refereed Journal Publications pertaining to this work

- Determination of the size of the dust torus in H0507+164 through optical and infrared monitoring

  A. K. Mandal, S. Rakshit, K. S. Kurian, C. S. Stalin, B. Mathew, R. Sagar, M. Pandge

  MNRAS, **475**, 5330- 5337, 2018

- REMAP: Determination of the inner edge of the dust torus in AGN by measuring time delays

  A. K. Mandal, S. Rakshit, I. Pal, C. S. Stalin, R. Sagar, B. Mathew

  Bulletin de la Société Royale des Sciences de Liège in Proceedings of the Second Belgo-Indian Network for Astronomy & Astrophysics (BINA) workshop, **88**, 158-165, 2019

- Quasar catalogue for the astrometric calibration of the forthcoming ILMT survey

  A. K. Mandal, B. Pradhan, J. Surdej, C. S. Stalin, R. Sagar, B. Mathew

  Accepted in *Journal of Astrophysics & Astronomy* (https://arxiv.org/abs/2007.07157)

- Estimation of the size and structure of the Broad Line Region in AGN using Bayesian approach

  A. K. Mandal, S. Rakshit, C. S. Stalin, R. G. Petrov, B. Mathew, R. Sagar

  Submitted to *MNRAS*, under review

- Dust Reverberation Mapping of Z229−15

  A. K. Mandal, S. Rakshit, C. S. Stalin, D. Wylezalek, M. K. Patig, R. Sagar, B. Mathew, S. Muneer, I. Pal

  Submitted to *MNRAS*

Additional Refereed Journal Publications

- Gamma-Ray-emitting Narrow-line Seyfert 1 Galaxies in the Sloan Digital Sky Survey

  S. Paliya Vaidehi, M. Ajello, S. Rakshit, **A. K. Mandal**, C. S. Stalin, A. Kaur, D. Hartmann

  ApJL, **853**, 2P, 2018

- Temporal correlation between the optical and γ-ray flux variations in the blazar 3C 454.3

  B. Rajput, C. S. Stalin, S. Sahayanathan, S. Rakshit, **A. K. Mandal**

  MNRAS, **486**, 1781-1795, 2019

Report Article

Centre for Research, CHRIST (Deemed to be University)

- Near Infrared JHKs observations of the transient MAXI J1820+070 / ASASSN-18ey
  A. K. Mandal, A. Singh, C. S. Stalin, S. Chandra, P. Gandhi
  ATel, **11462**, 1M, 2018

Articles under preparation related to this work

- Black hole mass measurement of Changing-look AGN Mrk 590 using Photometric Reverberation Mapping
  A. K. Mandal, S. Rakshit, C. S. Stalin, B. Mathew, R. Sagar
  MNRAS

Seminars/ Conferences/ Workshops attended

- Participated international conference on "Extragalactic Relativistic Jets: Cause and Effect " organised by ICTS in October, 2015.

- Participated in the Astronomical Society of India meeting; presented a poster on 'Determination of the size of the dust torus in H0507+164 through Optical-IR monitoring' at B.M. Birla Auditorium, Jaipur, India in March, 2017.

- Participated in the Young Astronomers' Meet (YAM), 2017 at IUCAA; presented a poster on 'Determination of the size of the dust torus in H0507+164 through Optical-IR monitoring' in September, 2017.

- Participated in Belgo-Indian Network for Astronomy & Astrophysics (BINA) (09 − 12 October, 2018) at Royal Observatory of Belgium, Brussels, Belgium, presented contributory talk on 'REMAP: Reverberation Mapping of Active galactic nuclei Program'.

- February, 2019 Participated in the Astronomical Society of India meeting, presented contributory talk on 'Estimation of the size and structure of the BLR region using Bayesian approach' at CHRIST (Deemed to be University), Bangalore.

- Attended in the meeting "Recent Trends in the Study of Compact Objects: Theory and Observation (RETCO-IV)" during 17 − 20 April, 2019 at IUCAA, Pune and presented a poster on "Reverberation measurement of the extent of the dust torus in AGN".

Centre for Research, CHRIST (Deemed to be University)

- Participated international conference on "Mapping Central Regions of Active Galactic Nuclei" held in Guilin, China during 19-24 September, 2019: presented a contributory talk on "Echo Mapping of Active Galactic Nuclei".

- Attended an online international workshop "ILMT - International Liquid Mirror Telescope Workshop" conducted by Aryabhatta Research Institute of Observational Sciences (ARIES), Nainital, India during 29 June - 01 July, 2020 and presented a contributory talk on "Astrometric calibration of ILMT fields: selection of calibrators and applications".

Centre for Research, CHRIST (Deemed to be University)

REFERENCES

Andjelić M., Stavrev K., Arbutina B., Ilić D., Urošević D., 2011, Baltic Astronomy, 20, 459

Antonucci R., 1993, ARA&A, 31, 473

Barth A. J., et al., 2011, ApJ, 732, 121

Barth A. J., et al., 2013, ApJ, 769, 128

Barvainis R., 1987, ApJ, 320, 537

Bentz M. C., Katz S., 2015, PASP, 127, 67

Bentz M. C., et al., 2006, ApJ, 651, 775

Bentz M. C., Peterson B. M., Netzer H., Pogge R. W., Vestergaard M., 2009, ApJ, 697, 160

Bentz M. C., et al., 2010, ApJ, 720, L46

Bentz M. C., et al., 2013, ApJ, 767, 149

Bessell M. S., Castelli F., Plez B., 1998, A&A, 333, 231

Bevington P. R., Robinson D. K., 1992, Data reduction and error analysis for the physical sciences

Blandford R. D., McKee C. F., 1982, ApJ, 255, 419

Bovy J., et al., 2011, The Astrophysical Journal, 729, 141

Brewer B. J., et al., 2011, ApJ, 733, L33

Carilli C. L., Perley R. A., Dhawan V., Perley D. A., 2019, ApJ, 874, L32

Collin S., Kawaguchi T., Peterson B. M., Vestergaard M., 2006, A&A, 456, 75

Czerny B., Hryniewicz K., Maity I., Schwarzenberg-Czerny A., Życki P. T., Bilicki M., 2013, A&A, 556, A97

Denney K. D., et al., 2010, ApJ, 721, 715

Du P., et al., 2014, ApJ, 782, 45

Du P., et al., 2016, ApJ, 825, 126

Du P., et al., 2018, ApJ, 856, 6

Edelson R. A., Krolik J. H., 1988, ApJ, 333, 646

Edelson R., Turner T. J., Pounds K., Vaughan S., Markowitz A., Marshall H., Dobbie P., Warwick R., 2002, ApJ, 568, 610

Ehlers J., Schneider P., 1992, Gravitational Lensing. p. 1, doi:10.1007/3-540-56180-3_1

Fabian A. C., 1999, Proceedings of the National Academy of Science, 96, 4749

Flesch E. W., 2017, VizieR Online Data Catalog, p. VII/280

GRAVITY Collaboration et al., 2019, arXiv e-prints, p. arXiv:1910.00593

Gaia Collaboration et al., 2018, A&A, 616, A14

Gaskell C. M., Peterson B. M., 1987, ApJS, 65, 1

Gaskell C. M., Sparke L. S., 1986, ApJ, 305, 175

Graham M., Djorgovski S. G., Stern D., Drake A. J., Mahabal A. A., Glikman E., 2016, in American Astronomical Society Meeting Abstracts #227. p. 243.40

Gravity Collaboration et al., 2018, Nature, 563, 657

Gravity Collaboration et al., 2020, A&A, 635, A92

Grier C. J., et al., 2013, ApJ, 764, 47

Grier C. J., Pancoast A., Barth A. J., Fausnaugh M. M., Brewer B. J., Treu T., Peterson B. M., 2017a, ApJ, 849, 146

Grier C. J., et al., 2017b, ApJ, 851, 21

Haas M., Chini R., Ramolla M., Pozo Nuñez F., Westhues C., Watermann R., Hoffmeister V., Murphy M., 2011, A&A, 535, A73

Ho L. C., Kim M., 2014, ApJ, 789, 17

Hönig S. F., Kishimoto M., 2017, ApJ, 838, L20

Hönig S. F., Watson D., Kishimoto M., Hjorth J., 2014, Nature, 515, 528

Kelly B. C., Bechtold J., Siemiginowska A., 2009, ApJ, 698, 895

Kim M., Ho L. C., Peng C. Y., Barth A. J., Im M., 2017, ApJS, 232, 21

Kishimoto M., Hönig S. F., Beckert T., Weigelt G., 2007, A&A, 476, 713

Centre for Research, Christ University, Bengaluru

Kishimoto M., Antonucci R., Blaes O., Lawrence A., Boisson C., Albrecht M., Leipski C., 2008, Nature, 454, 492

Kishimoto M., Hönig S. F., Antonucci R., Kotani T., Barvainis R., Tristram K. R. W., Weigelt G., 2009, A&A, 507, L57

Kishimoto M., Hönig S. F., Antonucci R., Barvainis R., Kotani T., Tristram K. R. W., Weigelt G., Levin K., 2011a, A&A, 527, A121

Kishimoto M., Hönig S. F., Antonucci R., Millour F., Tristram K. R. W., Weigelt G., 2011b, A&A, 536, A78

Kobayashi Y., Sato S., Yamashita T., Shiba H., Takami H., 1993, ApJ, 404, 94

Koshida S., et al., 2014, ApJ, 788, 159

Li Y.-R., Wang J.-M., Ho L. C., Du P., Bai J.-M., 2013, ApJ, 779, 110

Li Y.-R., Wang J.-M., Hu C., Du P., Bai J.-M., 2014, The Astrophysical Journal, 786, L6

Li Y.-R., et al., 2018, ApJ, 869, 137

Li Y.-R., Zhang Z.-X., Jin C., Du P., Cui L., Liu X., Wang J.-M., 2019, arXiv e-prints, p. arXiv:1909.04511

Lindegren L., Lammers U., Hobbs D., O'Mullane W., Bastian U., Hernández J., 2012, A&A, 538, A78

Lira P., Arévalo P., Uttley P., McHardy I., Breedt E., 2011, MNRAS, 415, 1290

Lynden-Bell D., 1969, Nature, 223, 690

Lyu J., Rieke G. H., Smith P. S., 2019, ApJ, 886, 33

Mandal A. K., et al., 2018, MNRAS, 475, 5330

Mandal A. K., Rakshit S., Pal I., Stalin C. S., Sagar R., Mathew B., 2019, Bulletin de la Societe Royale des Sciences de Liege, 88, 158

Marrese P. M., Marinoni S., Fabrizio M., Altavilla G., 2019, A&A, 621, A144

Meusinger H., Hinze A., de Hoon A., 2011, A&A, 525, A37

Minezaki T., et al., 2019, ApJ, 886, 150

Myers A. D., et al., 2015, ApJS, 221, 27

Narayan R., Bartelmann M., 1999, in Dekel A., Ostriker J. P., eds, Formation of Structure in the Universe. p. 360

Ninan J. P., et al., 2014, Journal of Astronomical Instrumentation, 3, 1450006

Oknyanskij V. L., Horne K., 2001, in Peterson B. M., Pogge R. W., Polidan R. S., eds, Astronomical Society of the Pacific Conference Series Vol. 224, Probing the Physics of Active Galactic Nuclei. p. 149

Oknyanskij V. L., Lyuty V. M., Taranova O. G., Shenavrin V. I., 1999, Astronomy Letters, 25, 483

Onken C. A., Ferrarese L., Merritt D., Peterson B. M., Pogge R. W., Vestergaard M., Wandel A., 2004, ApJ, 615, 645

Pancoast A., Brewer B. J., Treu T., 2011, ApJ, 730, 139

Pancoast A., et al., 2012, ApJ, 754, 49

Pancoast A., Brewer B. J., Treu T., Park D., Barth A. J., Bentz M. C., Woo J.-H., 2014, MNRAS, 445, 3073

Peng C. Y., Ho L. C., Impey C. D., Rix H.-W., 2002, AJ, 124, 266

Peters C. M., et al., 2015, ApJ, 811, 95

Peterson B. M., 1993, PASP, 105, 247

Peterson B. M., Horne K., 2004, Astronomische Nachrichten, 325, 248

Peterson B. M., Wanders I., Horne K., Collier S., Alexander T., Kaspi S., Maoz D., 1998, PASP, 110, 660

Peterson B. M., et al., 2004, ApJ, 613, 682

Petrov R. G., Millour F., Lagarde S., Vannier M., Rakshit S., Marconi A., weigelt G., 2012, in Optical and Infrared Interferometry III. p. 84450W (arXiv:1410.3108), doi:10.1117/12.926595

Pozo Nuñez F., et al., 2014, A&A, 561, L8

Rakshit S., Petrov R. G., Meilland A., Hönig S. F., 2015, MNRAS, 447, 2420

Rani P., Stalin C. S., Rakshit S., 2017, MNRAS, 466, 3309

Rashed Y. E., Eckart A., Valencia-S. M., García-Marín M., Busch G., Zuther J., Horrobin M., Zhou H., 2015, MNRAS, 454, 2918

Rathna Kumar S., Stalin C. S., Prabhu T. P., 2015, A&A, 580, A38

Refsdal S., 1964, MNRAS, 128, 307

Richards G. T., et al., 2002, AJ, 123, 2945

Richards G. T., et al., 2009, ApJS, 180, 67

Centre for Research, Christ University, Bengaluru

Richards G. T., et al., 2015, VizieR Online Data Catalog, p. J/ApJS/219/39

Salpeter E. E., 1964, ApJ, 140, 796

Sanders D. B., Phinney E. S., Neugebauer G., Soifer B. T., Matthews K., 1989, ApJ, 347, 29

Schnülle K., Pott J. U., Rix H. W., Peterson B. M., De Rosa G., Shappee B., 2015, A&A, 578, A57

Shakura N. I., Sunyaev R. A., 1973, A&A, 500, 33

Shen Y., et al., 2015, VizieR Online Data Catalog, 180

Souchay J., et al., 2015, A&A, 583, A75

Stalin C. S., Jeyakumar S., Coziol R., Pawase R. S., Thakur S. S., 2011, MNRAS, 416, 225

Suganuma M., et al., 2006, ApJ, 639, 46

Surdej J., et al., 2018, Bulletin de la Societe Royale des Sciences de Liege, 87, 68

Tomita H., et al., 2006, ApJ, 652, L13

Ulrich M.-H., Horne K., 1996, MNRAS, 283, 748

Ulrich M.-H., Maraschi L., Urry C. M., 1997, ARA&A, 35, 445

Urry C. M., Padovani P., 1995, PASP, 107, 803

Vaughan S., Edelson R., Warwick R. S., Uttley P., 2003, MNRAS, 345, 1271

Wagner S. J., Witzel A., 1995, ARA&A, 33, 163

Wandel A., Peterson B. M., Malkan M. A., 1999, ApJ, 526, 579

Wang J.-M., et al., 2014, ApJ, 793, 108

Watson D., Denney K. D., Vestergaard M., Davis T. M., 2011, ApJ, 740, L49

Welsh W. F., 1999, PASP, 111, 1347

Wilhite B. C., Vanden Berk D. E., Kron R. G., Schneider D. P., Pereyra N., Brunner R. J., Richards G. T., Brinkmann J. V., 2005, ApJ, 633, 638

Williams P. R., et al., 2018, ApJ, 866, 75

Woo J.-H., Yoon Y., Park S., Park D., Kim S. C., 2015, ApJ, 801, 38

Xiao M., et al., 2018, ApJ, 864, 109

Yoshii Y., Kobayashi Y., Minezaki T., Koshida S., Peterson B. A., 2014, ApJ, 784, L11

Zu Y., Kochanek C. S., Peterson B. M., 2011, ApJ, 735, 80

Centre for Research, Christ University, Bengaluru